Research Square

Preprints are preliminary reports that have not undergone peer review.
They should not be considered conclusive, used to inform clinical practice,
or referenced by the media as validated information.

Deciphering MMP9-Driven Mechanisms Underlying Rapid Antidepressant Effects from the Perspective of Neutrophil Homeostasis

Xia Li
State Key Laboratory of National Security Specially Needed Medicines
Tong Xu
State Key Laboratory of National Security Specially Needed Medicines
Tianze Zhou
State Key Laboratory of National Security Specially Needed Medicines
Weina Guo
State Key Laboratory of National Security Specially Needed Medicines
Ziyi Wang
State Key Laboratory of National Security Specially Needed Medicines
Jingcao Li
State Key Laboratory of National Security Specially Needed Medicines
Qiongyin Fan
State Key Laboratory of National Security Specially Needed Medicines
Shuo Li
State Key Laboratory of National Security Specially Needed Medicines
Shuaiming Zhu
State Key Laboratory of National Security Specially Needed Medicines
Yang Zhang
State Key Laboratory of National Security Specially Needed Medicines
Rui Xue
State Key Laboratory of National Security Specially Needed Medicines
Youzhi Zhang
bcczyz@163.com

State Key Laboratory of National Security Specially Needed Medicines

Research Article

Keywords: Depression, Neutrophils, MMP9, Rapid-acting antidepressant, Blood-brain barrier, Neuronal plasticity

Posted Date: November 9th, 2026

DOI: https://doi.org/10.21203/rs.3.rs-11420917/v1

License: This work is licensed under a Creative Commons Attribution 4.0 International License.
Read Full License

Additional Declarations: No competing interests reported.

Deciphering MMP9-Driven Mechanisms Underlying Rapid Antidepressant Effects from the Perspective of Neutrophil Homeostasis

Xia Li[a], Tong Xu[a], Tianze Zhou[a], Weina Guo[a], Ziyi Wang[a], Jingcao Li[a], Qiongyin Fan[a], Shuo Li[a], Shuaiming Zhu[a], Yang Zhang[a], Rui Xue[a,*], Youzhi Zhang[a,*]

[a]State Key Laboratory of National Security Specially Needed Medicines, Beijing, 100039, China

*Corresponding author. Rui Xue, State Key Laboratory of National Security Specially Needed Medicines, Beijing, 100039, China. Tel.: +86-010-66930629; e-mail: hly19830718@sina.com

*Corresponding author. Youzhi Zhang, State Key Laboratory of National Security Specially Needed Medicines, Beijing, 100039, China. Tel.: +86-010-66874620; e-mail: bcczyz@163.com

Abstract

Background: Depression exhibits marked clinical heterogeneity, and peripheral neutrophil functional status is closely associated with disease progression and treatment response; however, its role in rapid antidepressant action remains poorly understood.**Methods:** Taking neutrophil homeostasis as the entry point, this study integrated single-cell transcriptomic sequencing, primary cell functional assays, a Transwell in vitro blood–brain barrier (BBB) model, and three mouse models of depression with distinct neutrophil functional states to systematically dissect the immune mechanism by which matrix metalloproteinase-9 (MMP9) mediates rapid antidepressant effects.**Results:** The results showed that MMP9 originates predominantly from peripheral neutrophils, whereas brain-resident cells exhibit extremely low basal expression that cannot be substantially upregulated by drug stimulation. The rapid-acting antidepressants 2,5-dimethoxy-4-methylamphetamine (DOM) and ketamine (KET) activate phosphoinositide 3-kinase-protein kinase B (PI3K-Akt) signaling in neutrophils, driving polarization toward an N2 anti-inflammatory phenotype with a moderate upregulation of MMP9 expression. Under

neutrophil-homeostatic conditions, MMP9 crosses the BBB via caveolin-1-mediated transcytosis in endothelial cells, without disrupting tight junctions or relying on neutrophil brain infiltration. Upon entering the brain, MMP9 degrades perineuronal nets (PNNs), restores dendritic–spine plasticity, and recovers gamma-oscillation circuit function, thereby mediating rapid antidepressant effects. Notably, therapeutic efficacy was strictly dependent on neutrophil functional status: suppression of neutrophil function depleted peripheral MMP9 supply and markedly attenuated drug responses, which could be rescued by hippocampal MMP9 replenishment; whereas hyperactivation of neutrophils generated excessive, neurotoxic MMP9, and inhibiting MMP9 activity restored drug sensitivity.**Conclusions:** These findings indicate that neutrophil-derived MMP9 is a key effector molecule linking peripheral immune status to central rapid antidepressant efficacy, and provide an experimental basis and novel molecular targets for neutrophil-state-based immune subtyping of depression and individualized precision intervention.

Keywords: Depression; Neutrophils; MMP9; Rapid-acting antidepressant; Blood-brain barrier; Neuronal plasticity

1 Introduction

Depression constitutes a significant mental health disorder that poses serious risks to both physical and psychological well-being[1]. It is marked by its high prevalence, notable recurrence rates, and considerable disability impacts, making it a pressing public health concern on a global scale that demands immediate attention[2]. Data from the World Health Organization (WHO) indicates that around 320 million individuals across the globe are affected by depression, reflecting a continuously growing burden of this disease[3]. Restricted by multiple practical factors including stigma and insufficient disease recognition, the actual clinical consultation rate of depression remains far lower than its population prevalence[4]. Meanwhile, this disease is closely associated with social competitive pressure, altered lifestyles and population aging[5]. Adolescents, high-stress occupational groups and the elderly represent high-risk populations with markedly elevated suicide risk; up to 15% of patients with major depressive disorder die by suicide, imposing a heavy burden on families and society[6].

First-line clinical antidepressants are represented by selective serotonin reuptake inhibitors (SSRIs) and serotonin-norepinephrine reuptake inhibitors (SNRIs)[7]. Nevertheless, current therapeutic regimens still exhibit notable limitations. Clinical medication largely relies on empirical symptom-based diagnosis, lacking individualized treatment strategies supported by biological subtyping[8]. Conventional antidepressants generally feature a 4–6 week therapeutic delay, prolonging patients' suffering and increasing the risk of early treatment dropout[9]. Moreover, the overall response rate of first-line agents is merely ~60%, with an even smaller proportion of patients achieving full clinical remission; numerous patients experience persistent and recurrent symptoms[10,11]. Accordingly, deciphering the pathophysiological basis underlying depression heterogeneity, screening biomarkers for subtype discrimination, and advancing stratified precision management and individualized intervention constitute critical scientific goals in this field[12].

Aberrant neuro-immune crosstalk represents a key research frontier for the pathogenesis of depression[13]. As core innate immune effector cells, neutrophils have attracted growing attention regarding their roles in the onset and progression of depression[14]. Dominant classical theories are built upon high-inflammatory depression models: chronic stress activates the neuroendocrine-immune axis, prompting bone marrow mobilization and neutrophil release[15], accompanied by inflammatory phenotypes such as elevated peripheral neutrophil-to-lymphocyte ratio (NLR)[16]. Activated neutrophils release neutrophil extracellular traps (NETs) to disrupt the blood-brain barrier (BBB) and mediate central neuroinflammation[17]. For this high-inflammatory subtype, combinatorial administration of anti-inflammatory agents alongside classic antidepressants has been proposed[18]. However, clinical cohort and epidemiological evidence indicates that this theory applies only to a subset of patients: approximately one-quarter of individuals with depression exhibit low-grade inflammation (CRP > 3 mg/L)[19], whereas in the remaining patients, peripheral inflammatory markers, despite statistically significant mild elevations, mostly remain within clinical reference ranges[20]. Notably, elevated baseline inflammation has been associated with poor response to traditional antidepressants such as SSRIs and with treatment resistance,

suggesting that peripheral inflammatory status may facilitate the biological subtyping of depression[21]. Furthermore, an easily overlooked subgroup of patients with depression presents with reduced neutrophil counts or impaired neutrophil function. This phenotype can arise secondary to conditions such as bone marrow suppression following radiotherapy or chemotherapy, malnutrition, and infection[22], and may contribute to the pathogenesis of depression through the gut–brain axis and neuroendocrine pathways[23]. Nevertheless, systematic investigations into the pathological mechanisms and intervention strategies for neutrophil-suppressed depression remain scarce[14]. Taken together, these findings lead us to propose that depression may be classified, according to peripheral neutrophil functional status, into three immune subtypes, neutrophil-activated, neutrophil-homeostatic, and neutrophil-suppressed, which differ substantially in etiology and treatment response. The key effector molecules mediating the phenotypic differences among these subtypes remain to be elucidated[12,13].

Matrix metalloproteinase-9 (MMP9), a zinc-dependent endopeptidase originally identified in neutrophils[24], functions in extracellular matrix remodeling and synaptic plasticity regulation, and has garnered widespread interest for its roles in neuropsychiatric disorders[25]. Under physiological conditions, MMP9 participates in nervous system development, synaptic remodeling, learning and memory[26,27]. Pathologically, dysregulated MMP9 activity contributes to neurodegeneration, inflammatory injury and tumorigenesis[28]. Early studies primarily focused on the detrimental effects of MMP9 under excessive inflammatory conditions, demonstrating that high MMP9 expression degrades tight junction proteins, exacerbates BBB breakdown and amplifies neuroinflammation[29,30]. Cumulative recent evidence, however, reveals a dual biological role of MMP9. Moderate MMP9 activation cleaves pro-BDNF to generate mature BDNF[31], degrades perineuronal nets (PNNs), modulates the function of PV-positive interneurons, improves gamma oscillations, and participates in neuroplasticity restoration induced by rapid-acting antidepressants[32,33]. Consistent evidence indicates that neutrophils are the predominant source of circulating MMP9, which is stored as a zymogen in neutrophil tertiary (gelatinase) granules and released

rapidly via degranulation upon inflammatory stimulation (IL-8, TNF-α, and LPS); circulating MMP9 levels therefore closely track neutrophil abundance and activation status[34]. This relationship has been observed across diverse disease models. Peripheral MMP9 rises markedly during the early phase of sepsis and endotoxemia[35]; in autoimmune diseases such as rheumatoid arthritis, activated neutrophils accumulate in the synovium and release MMP9 through neutrophil extracellular traps (NETs), contributing to cartilage matrix degradation[36,37]; and under chemotherapy- or radiotherapy-induced myelosuppression, circulating MMP9 declines in parallel with neutrophil counts, whereas granulocyte colony-stimulating factor (G-CSF)-induced neutrophil mobilization is accompanied by increased MMP9[38].

Two major scientific controversies persist regarding MMP9 in depression research. Elucidating the authentic functions, cellular sources, and functional boundaries of MMP9 in depression is critical to deciphering the mechanisms underlying rapid-acting antidepressants, explaining disease heterogeneity, and advancing biomarker-guided stratified therapy[33]. The first controversy centers on cellular sources. Some studies propose that central neurons, astrocytes, and microglia represent the primary resident sources of brain MMP9 synthesis[39], whereas other evidence identifies peripheral neutrophils as the major contributors[34]. Brain MMP9 can originate from in situ synthesis or peripheral transport[34,39]. Systematic validation remains absent to determine whether the dominant source of MMP9 shifts under distinct pathological conditions. The second controversy concerns its dual functionality. MMP9 mediates neuroprotective effects and facilitates synaptic remodelling, yet excessive MMP9 activation induces aberrant extracellular matrix degradation and BBB disruption[29,32]. Reports describing MMP9 regulation by rapid-acting antidepressants vary across animal models and inflammatory contexts[31,33]. These observations indicate that MMP9 exerts complex functions tightly coupled to antidepressant responses. Further work is warranted to explore whether a beneficial concentration range exists for MMP9 protein and how such a range correlates with neutrophil status[34].

In terms of pharmacological tools, two classes of interventions with distinct

pharmacological mechanisms yet equally rapid onset provide a natural comparative framework for examining the pivotal questions raised above. The first class is represented by ketamine (KET). As an NMDA receptor antagonist, its rapid antidepressant effect, which emerges within hours after a single administration, has been well established[40,41], making ketamine the prototypical rapid acting antidepressant. Its S enantiomer esketamine was approved by the FDA in 2019 for treatment resistant depression and remains one of the few rapid onset antidepressants currently available on the market[42]. Moreover, the therapeutic efficacy of ketamine has been shown to depend in part on MMP9 mediated remodeling of the extracellular matrix and perineuronal nets (PNNs)[33], and animal studies indicate that ketamine rapidly alters PNN integrity in concert with MMP9 associated plasticity events[32]. However, a single low dose ketamine infusion in the clinic did not significantly alter peripheral MMP9 levels in patients[43], pointing to a critical gap in our understanding of the temporal sequence and causal relationships underlying the peripheral origin versus central action of MMP9, as well as its short term benefit versus long term cost. The second class is represented by amphetamine type psychedelics. Acting as 5-HT2A receptor agonists, these compounds rapidly promote dendritogenesis, spinogenesis, and synaptogenesis in prefrontal pyramidal neurons, an onset profile that closely resembles the rapid antidepressant paradigm[44]. The antidepressant potential of this pharmacological class is attracting growing attention. Psilocybin, a classic psychedelic that likewise acts as a 5-HT2A receptor agonist, has demonstrated rapid and sustained antidepressant effects in randomized controlled trials. In a phase 2 trial its efficacy was non inferior to escitalopram[45], and in the phase 3 COMP360 trial it met the primary endpoint, with symptom improvement apparent the day after a single administration and lasting for weeks, a profile that has earned it FDA breakthrough therapy designation[46]. lysergic acid diethylamide (LSD) has also shown exploratory potential for antidepressant application in early clinical and translational studies, although randomized controlled evidence remains to be established[47]. Nevertheless, chronic or high dose use of amphetamine type compounds can lead to addiction and exacerbate systemic inflammation[48]. Given that neutrophils serve as the principal reservoir and release source of circulating

MMP9[24,34,38], and that MMP9 has been implicated in amphetamine induced inflammation[49], whether short term low dose administration of amphetamine type compounds can moderately upregulate MMP9 without excessively activating neutrophils, and thereby yield therapeutic benefit, remains an open question that bears directly on the benefit risk balance of these drugs. Accordingly, this study employs KET and the amphetamine derivative 2,5-dimethoxy-4-methylamphetamine (DOM) as pharmacological tools to dissect the antidepressant mechanism of MMP9, and examines, within a unified experimental framework, the effects of these two rapid onset drugs, which differ markedly in their addiction and inflammation risk profiles, on neutrophil functional status, peripheral MMP9 supply, and blood brain barrier transport.

Based on literature review and preliminary experimental data, we propose the following hypothesis: depression can be categorized into three immune subtypes (activated, homeostatic and suppressed) according to neutrophil functional status[13,19]. Peripheral neutrophils constitute the primary source of MMP9[34,38], which mediates the therapeutic effects of rapid-acting antidepressants DOM and KET, and drug efficacy depends on host neutrophil functional status[32,33]. Under homeostatic neutrophil conditions in depression, moderate MMP9 upregulation mediates rapid antidepressant effects[31]. Excess MMP9 induces neurotoxicity and attenuates drug efficacy when neutrophils are overactivated[30]. When neutrophil function is suppressed, insufficient peripheral MMP9 supply compromises therapeutic responses, necessitating MMP9-targeted interventions[22]. This study aims to systematically validate this hypothesis by integrating in vitro cellular models, Transwell BBB systems and multiple depressive animal models, and dissect the molecular mechanisms by which neutrophil-derived MMP9 contributes to rapid antidepressant actions[12]. Findings from this work are expected to provide experimental evidence for biological subtyping of depressive immune subtypes, and offer novel molecular targets and theoretical support for individualized precision intervention with rapid-acting antidepressants.

2 Materials and Methods

2.1 Experimental Animals

In this study, all in vivo animal experiments involved 8-week-old male C57BL/6J mice of SPF grade, which were obtained from Beijing HFK Bioscience Co., Ltd. All subjects were maintained in an SPF animal facility with regulated conditions: a temperature range of 22–24 °C, relative humidity maintained at 50%–60%, a circadian rhythm comprising 12 hours of light followed by 12 hours of darkness, regular cage changes, and unrestricted access to standard chow along with sterile water. All procedures involving animals adhered to the protocols sanctioned by the Institutional Animal Care and Use Committee (IACUC-DWZX-2025-601) at the National Key Laboratory of National Security Special Medicines, and handling of the animals conformed to the 3R principles governing laboratory animal ethics[50].

2.1.1 Animal Model Establishment

LPS-induced acute inflammatory depression model: 8-week-old male C57BL/6J mice were acclimatized for 7 days. Mice in the model group received intraperitoneal injection of lipopolysaccharide (LPS, 1 mg/kg, dissolved in sterile saline; Sigma-Aldrich, Cat. L2630-25MG, derived from *Escherichia coli* O111:B4, stored at 2–8 °C), whereas the control group received an equal volume of sterile saline. A full battery of behavioral tests was performed 10 h after administration, followed by peripheral blood collection and hippocampal tissue dissection for molecular biology, flow cytometry and single-cell transcriptomic sequencing assays[51].

Neutrophil activation model was established by chronic low-dose LPS stimulation. Eight-week-old male C57BL/6J mice were intraperitoneally injected with LPS (0.3 mg/kg) every other day for 14 consecutive days; the control group received an equal volume of sterile saline. Behavioral assessments were conducted upon model completion, and peripheral blood was collected to detect inflammatory markers including neutrophils (NEU), neutrophil-to-lymphocyte ratio (NLR), and C-reactive protein (CRP). An additional MMP9 inhibitor (MMP9-IN-1) intervention group was set up, in which MMP9-IN-1 (15 mg/kg) was administered intraperitoneally synchronously with LPS modeling to observe the rescue effects of MMP9 inhibition on animal phenotypes[52].

Neutrophil suppression model: peripheral neutrophil depletion was achieved by

intraperitoneal injection of the neutrophil-specific neutralizing antibody anti-LY6G (1 mg/kg, dissolved in sterile PBS) every other day for 14 consecutive days[53]. Retro-orbital blood sampling was performed after modeling, and routine blood tests were used to verify the efficiency of peripheral neutrophil depletion. Stereotaxic injection of AAV-MMP9 virus into the hippocampal dentate gyrus (DG) region was performed to achieve local hippocampal MMP9 overexpression for phenotypic rescue of neutrophil depletion-induced depressive-like behaviors.

Chronic restraint stress (CRS) neutrophil-homeostatic depression model. Mice were placed in 50 mL ventilated restraint tubes and subjected to 6 h of daily restraint stress for 14 consecutive days[54]. Retro-orbital blood was collected after modeling for routine blood analysis, and individuals with peripheral neutrophil counts outside the normal physiological range were excluded to obtain CRS depression mice with neutrophil homeostasis. Two composite models were constructed. The CRS+LPS neutrophil-activated depression model was CRS modeling combined with intraperitoneal injection of low-dose LPS (0.3 mg/kg) every other day for 14 days. The CRS+anti-LY6G neutrophil-suppressed depression model was CRS modeling combined with intraperitoneal injection of anti-LY6G (1 mg/kg) every other day for 14 days.

Stereotaxic hippocampal AAV virus injection: mice were anesthetized with isoflurane (induction 3%–4%, maintenance 1.5%–2%) and fixed in a stereotaxic frame (RWD Life Science). The scalp was disinfected, and a midline cranial incision was made to expose the skull. The hippocampal DG region was localized according to *The Mouse Brain in Stereotaxic Coordinates* (Paxinos & Franklin, 2nd edition): bregma −2.06 mm, ±1.5 mm lateral to midline, −2.0 mm below the dura mater. A ~0.5 mm diameter craniotomy hole was drilled. A glass micropipette (tip diameter 10–30 μm) coupled with a microinjection pump was used for slow infusion of AAV-MMP9 virus (titer $\geq 1\times10^{12}$ vg/mL), with 250 nL injected per hippocampus at a rate of 20 nL/min. The pipette was retained for 5 min after injection and withdrawn slowly at 0.2 mm/min. The scalp was sutured, and mice were placed on a heating pad for recovery for 3 weeks to allow sufficient viral expression prior to subsequent modeling, drug administration and sample detection[55].

2.1.2 In Vivo Drug Administration Regimen

2,5-dimethoxy-4-methylamphetamine (DOM), ketamine (KET), and fluoxetine (FLX) were obtained from State Key Laboratory of National Security Specially Needed Medicines, with purity ≥98%. DOM (0.5 mg/kg), KET (10 mg/kg), and FLX (10 mg/kg) were dissolved in sterile saline and administered via a single intraperitoneal injection at an injection volume of 10 mL/kg[56]. MMP9-IN-1 (MedChemExpress, Cat. HY-135232) inhibitor was formulated at the appropriate concentration according to the manufacturer's instructions and delivered intraperitoneally; vehicle control animals received an equal volume of corresponding solvent. Behavioral tests were performed 10 h post-administration, followed by tissue harvesting.

2.2 Cells, Plasmids, Antibodies and Major Reagents

2.2.1 Cell Lines

The bEnd.3 mouse brain microvascular endothelial cell line (ATCC, Cat. CRL-2299) was cultivated in complete medium, which consisted of high-glucose DMEM with added 10% fetal bovine serum (FBS) and 1% penicillin-streptomycin[57]. C8-D1A mouse astrocytes (ATCC, Cat. CRL-2535) were also grown as adherent cultures using the same complete medium as that for the bEnd.3 cells. The cells were incubated at 37 °C with 5% CO_2 in a humidified environment. Every 2–3 days, cells were passaged at a split ratio ranging from 1:3 to 1:4, and functional experiments or passaging occurred when the confluence reached 80%–90%. For cryopreservation, the medium consisted of the complete medium along with 10% DMSO, and cells were stored in liquid nitrogen for extended periods. A mycoplasma detection kit (Beyotime, Cat. C0302) was routinely used to check for contamination.

2.2.2 Primary Cell Isolation, Culture and Purity Validation

Primary mouse hippocampal neurons were isolated from C57BL/6J neonatal pups within 0–12 h after birth[58]. After surface disinfection with 75% ethanol, pups were decapitated, and hippocampi were aseptically dissected on ice in pre-chilled D-Hank's solution. Meninges and blood vessels were removed under a dissecting microscope. Tissues were minced into ~1 mm^3 fragments and digested with 0.25% trypsin (containing 0.02% EDTA) at 37 °C for 15 min with gentle agitation every 5 min. Digestion was terminated by DMEM containing 10% FBS. A fire-polished Pasteur pipette was used for gentle trituration (10–15 times) to prepare a

single-cell suspension, which was filtered through a 70 μm sterile cell strainer and centrifuged at 300 g for 5 min to collect cell pellets. Cells were seeded onto culture plates or coverslips pre-coated with 0.01 mg/mL poly-D-lysine (PDL) overnight at 37 °C. Neurons were cultured in Neurobasal medium supplemented with 2% B-27 supplement, 0.5 mM GlutaMAX-I and 1% penicillin-streptomycin. Cytosine arabinoside (Ara-C) was added at a final concentration of 5–10 μM 48 h after seeding to inhibit glial proliferation. Fresh medium was replaced 48 h later, followed by half-medium changes every 2–3 days. Neurons cultured for 7 days in vitro were used for experiments. Purity was characterized by MAP2 immunofluorescence and flow cytometry; preparations with MAP2-positive rate ≥90% were used for subsequent assays.

Primary B and T lymphocytes were isolated from sterile spleens of adult C57BL/6J mice. Spleens were rinsed with pre-cooled PBS, placed on a 70 μm cell strainer, and ground with a syringe plunger to prepare single-cell suspensions. Red blood cells were lysed with ACK lysis buffer (150 mmol/L NH_4Cl, 10 mmol/L $KHCO_3$, 0.1 mmol/L EDTA, pH 7.2) at room temperature for 5 min. Lysis was quenched with 10 volumes of pre-cooled PBS, followed by centrifugation and washing at 300 g. The RWD immunomagnetic bead sorting kits (Pan-B kit Cat. F1501-10; $CD3^+$ T cell kit Cat. K1301-10) were used according to the manufacturer's instructions: antibody incubation at 4 °C in the dark for 15 min and magnetic bead incubation for 10 min[59]. Purified B and T lymphocytes were obtained by negative selection on a magnetic stand. Sorting buffer: PBS (pH 7.2) supplemented with 0.5% BSA and 2 mM EDTA, filtered through a 0.22 μm membrane. B cells were labeled with CD19 and T cells with CD3; purity was verified by flow cytometry, and preparations with ≥95% purity were adopted.

Primary neutrophils were isolated using the Solarbio mouse peripheral blood neutrophil isolation kit (Cat. P9201)[60]. Fresh anticoagulated blood was collected from mouse orbits (sodium heparin final concentration 20 U/mL). Blood, dilution buffer and erythrocyte sedimentation buffer were mixed at a volume ratio of 1:1:1 and kept at room temperature for 30–40 min to sediment erythrocytes. The upper leukocyte-containing supernatant was overlaid onto an equal volume of separation medium while maintaining a sharp interface. Samples were centrifuged at 600–1000 g for 25–30 min at room temperature in a horizontal rotor with brake disabled. The milky white neutrophil layer was carefully aspirated, washed

twice with 3 volumes of washing buffer and centrifuged at 250 g for 10 min. Cells were resuspended in RPMI-1640 complete medium containing 10% FBS and 1% antibiotics. Cell viability ≥95% was confirmed by trypan blue staining. Neutrophils were isolated via magnetic bead sorting for $LY6G^+$ positivity, and those with purity ≥90 % were used for subsequent experiments. Flow cytometry was applied to quantify the proportion of positive cells for neutrophils, primary hippocampal neurons, B lymphocytes, astrocytes, T lymphocytes and microglia before and after isolation to evaluate purification efficiency (Figure S1).

2.2.3 Plasmids and Cell Transfection

Knockdown plasmids were purchased from Miaoling Bioscience: pLV3-U6-MMP9-shRNA1-mCherry-Blast (sh-MMP9, MMP9 knockdown). Primary neutrophils were transfected using Lipofectamine 3000 (Thermo Fisher, Cat. L3000015)[61]. Cells were seeded in 24-well plates one day before transfection at a density of $2–3\times10^5$ cells/well and reached 70%–90% confluence at transfection. According to the manufacturer's protocol, plasmid DNA (0.5–1 μg/well), P3000 reagent (1–2 μL/well) and Lipofectamine 3000 (1–1.5 μL/well) were diluted separately in Opti-MEM serum-free medium. After 5 min incubation at room temperature, plasmid-P3000 complexes were mixed with liposomes and incubated for 15–20 min to form transfection complexes, which were added dropwise to wells with gentle shaking. Complete medium was refreshed 4–6 h later. Twenty-four to 48 h after transfection, CopGFP/mCherry reporter fluorescence was visualized under a fluorescence microscope to assess transfection efficiency; samples with fluorescence positivity ≥50% were considered qualified. JESS capillary protein electrophoresis was used to validate knockdown efficiency, with ≥50% protein-level knockdown defined as the acceptance criterion.

2.2.4 Major Reagents, Antibodies and Kits

LPS (*E. coli* O111:B4, Cat. L2630-25MG) was purchased from Sigma-Aldrich. MMP9-IN-1 was from MCE (Cat. HY-13658). Anti-LY6G neutralizing antibody (clone 1A8, Cat.108414) and rat IgG2a isotype control antibody (Cat.400544) were obtained from BioLegend. AAV-MMP9 (AAV9 serotype, CMV promoter, titer $\geq1\times10^{12}$ vg/mL) was purchased from GeneChem.

Transwell culture inserts (Corning) with 0.4 μm pore size PET membrane (Cat. 3470)

were used for the in vitro co culture model of neutrophils and primary hippocampal neurons, and inserts with 3.0 μm pore size PET membrane (Cat. 3415) were applied for blood brain barrier construction. The Mindray BC-5180CRP automated five-part hematology analyzer was used for routine blood analysis and CRP detection in mouse peripheral blood, matched with M-53D diluent, M-5LEO lytic reagent and M-53P probe cleaning solution. Single-cell transcriptomic library construction was performed using the SeekOne® DD Single-Cell 3' Transcriptome Library Kit (Cytion Bio / SeekGene), coupled with the SeekOne® DD digital droplet system for single-cell capture and library preparation.

For protein lysis, RIPA buffer (Beyotime, Cat. P0013B) was supplemented freshly with protease inhibitor cocktail (MCE, Cat. HY-K0010, 100× dilution), 1 mM PMSF (Beyotime, ST506), and phosphatase inhibitor Na_3VO_4 (MCE, Cat. HY-K0092, 200× dilution). Protein quantification was performed using the BCA protein assay kit (Thermo Fisher, Cat. 23225). Capillary immunoassays were run on the ProteinSimple JESS automated capillary electrophoresis system with matching kits (PS-ST01-EZ-8, DM-001).

Primary antibodies include MMP9 (Proteintech, Cat. 10375-2-AP, 1:200); TrkB/NTRK2 (Proteintech, Cat. 13129-1-AP, 1:200); p-AKT (Ser473) (CST, Cat. 4060S, 1:100); AKT (CST, Cat. 4691S, 1:200); Claudin-1 (Proteintech, Cat. 28674-1-AP, 1:200); Claudin-5 (Proteintech, Cat. 29767-1-AP, 1:200); ZO-1 (Proteintech, Cat. 21773-1-AP, 1:100); Caveolin-1 (CST, Cat. 3267S, 1:200); TUBB3/β-III-tubulin (CST, Cat. 5568S, 1:500); BCAN (Abcam, Cat. ab224320, 1:200); BAX (Proteintech, Cat. 50599-2-Ig, 1:300); BCL-2 (Proteintech, Cat. 12789-1-AP, 1:300); GAPDH (Proteintech, Cat. 60004-1-Ig, 1:1000); PV/Parvalbumin (Abcam, Cat. ab11427, 1:500); PNN/Aggrecan (Abcam, Cat. ab3778, 1:200); MAP2 (Proteintech, Cat. 17490-1-AP, 1:500). Fluorescent secondary antibodies (Invitrogen): Alexa Fluor 488 donkey anti-rabbit IgG (Cat. A-21206, 1:500); Alexa Fluor 594 donkey anti-rabbit IgG (Cat. A-21207, 1:500); Alexa Fluor 488 donkey anti-mouse IgG (Cat. A-21202, 1:500).

Flow cytometry fluorophore-conjugated antibodies (BioLegend) include LY6G-FITC (Cat. 127608, 1:200), CD11b-APC (Cat. 101226, 1:200), CD19-PE (Cat. 115512, 1:200), CD3ε-FITC (Cat. 100312, 1:200), ACSA-2-APC (Cat. 154006, 1:200).

CCK-8 cell viability assay kit (Elabscience, Cat. E-CK-A362); FITC-Dextran (70 kDa,

Sigma-Aldrich) for barrier permeability measurement; FD Rapid GolgiStain™ kit (FD NeuroTechnologies, Cat. PK401); 4% paraformaldehyde (Servicebio, Cat. G1101); Triton X-100 (Sigma-Aldrich, Cat. T8787); BSA blocking buffer (Beyotime, Cat. ST023); DAPI (Invitrogen, Cat. D3571, final concentration 1 μg/mL); anti-fade mounting medium (SouthernBiotech, Cat. 0100-01).

2.3 In Vitro Model Establishment and Functional Assays

2.3.1 Transwell In Vitro Blood-Brain Barrier Co-Culture Model

An in vitro BBB model was constructed in 24-well plates using Transwell inserts with 3 μm PET membranes (Corning, Cat.3452). C8-D1A astrocytes were seeded in the basolateral lower chamber at $1–2\times10^4$ cells/cm²; bEnd.3 brain microvascular endothelial cells were seeded on the apical side of the insert membrane at $1–2\times10^5$ cells/cm². Co-culture proceeded at 37 °C with 5% CO_2 for 3–7 days, with half-volume medium renewal every 48 h[62]. Transendothelial electrical resistance (TEER) was measured daily with a Millicell ERS-2 volt-ohm meter (Millipore). The STX2 electrode was equilibrated in 0.15 mol/L NaCl solution, sterilized in 75% ethanol and rinsed with sterile PBS before use. Blank insert resistance was subtracted; the model was considered mature when TEER stabilized at approximately 120 Ω·cm². Neutrophil concentration gradients were set to include low density at 5×10^3/cm² for suppressed phenotype, medium density at 5×10^4/cm² for homeostatic phenotype, and high density at 5×10^5/cm² for activated phenotype. Freshly isolated neutrophils were added to the upper chamber, and samples were harvested after 10 h and 48 h co-incubation for subsequent detection.

CCK-8 viability assays were performed to screen in vitro working concentrations[63]. bEnd.3 cells were seeded in 96-well plates (1×10^4 cells/well) and allowed to attach overnight. Gradient concentrations of DOM (10^{-4} μM–10 μM), KET (10^{-3} μM–100 μM) and FLX (10^{-3} μM–100 μM) were applied for 24 h. A <10% reduction in cell viability after drug treatment was defined as the safety threshold, yielding final in vitro working concentrations: DOM 1 μM, KET 10 μM, FLX 10 μM. The integrity and function of the barrier were assessed by the following measurements. For TEER measurement, the culture plate was equilibrated at room temperature for 10 min before reading, the culture medium was replaced with

prewarmed PBS, and the fluid levels in the upper and lower chambers were equalized. The resistance was recorded once the reading remained stable for approximately 10 s, and the value in Ω·cm² was calculated after subtracting the resistance of a blank cell-free insert. For the FITC-dextran permeability assay, FITC-dextran (70 kDa) was added to the upper chamber at a final concentration of 1 mg/mL, and 100 μL of fluid was collected from the lower chamber at 1, 10, and 48 h, with an equal volume of prewarmed PBS replenished after each collection[64]. Fluorescence intensity was measured on a microplate reader at an excitation wavelength of 488 nm and an emission wavelength of 520 nm, and the relative permeability P/P_0 was calculated, where P_0 denotes the permeability of a cell-free blank insert. bEnd.3 cells were harvested from the upper insert and lysed with RIPA buffer, and the expression of the tight junction proteins Claudin-1 and Claudin-5 and of the transcytosis protein Caveolin-1 was quantified by JESS capillary electrophoresis. The continuity of endothelial tight junctions was evaluated by ZO-1 immunofluorescence staining (Fig.S2A-E). The medium from the lower chamber was collected to count neutrophils that had migrated to the basal side, and MMP9 protein levels were quantified by ELISA.

2.3.2 Non-Contact Transwell Co-Culture Model of Neutrophils and Primary Hippocampal Neurons

A non-contact co-culture system was established using Transwell inserts with 0.4 μm pore-size PET membranes (Corning, Cat. 3470)[65]. The upper chamber was seeded with wild-type or sh-MMP9-transfected primary neutrophils (48 h post-transfection) at 5,000–10,000 cells/well, while the lower chamber was pre-seeded with primary hippocampal neurons cultured for 7 days in vitro at a density of 20,000–30,000 cells/well (24-well plate). The semipermeable membrane permits free diffusion of proteins and cytokines but prevents cell transmigration, thereby achieving non-contact co-culture. Corresponding drugs (DOM 1 μM, KET 10 μM, FLX 10 μM) were added to the system for 12 h treatment; neurons in the lower chamber were then collected for protein extraction and JESS detection.

2.3.3 CCK-8 Cell Viability Assay

bEnd.3 or C8-D1A cells were plated in 96-well plates at a density of 5000–10,000 cells per well, with six biological replicates established for each group[63]. To minimize evaporation,

phosphate-buffered saline (PBS) filled the edge wells. Following a period of overnight attachment, the cells were subjected to treatments with drugs that were serially diluted. Each well received 10 microliters of CCK-8 working solution, after which the plates were incubated for 1–2 hours at 37 °C in the absence of light. Absorbance was measured at 450 nm while using 630 nm as the reference wavelength. The percentage of cell viability was calculated using the formula: Cell viability (%) = [(OD_{450} of the experimental group − blank OD_{450}) / (OD_{450} of the control group − blank OD_{450})] × 100%.

2.3.4 Microscale Thermophoresis (MST) Molecular Interaction Assay

Recombinant TrkB protein (Sino Biological, Cat.50459-M20B, purity ≥95%) was fluorescently labeled at the His-Tag using the NT.115 protein labeling kit (NanoTemper, Cat.MO-L011), with labeled protein at a final concentration of 50–200 nmol/L[66]. Serial 2-fold dilutions of DOM and KET were prepared with 16 concentration points and a maximum concentration of 1 mmol/L. Detection was performed on a Monolith NT.115 instrument at 25 °C. Samples were loaded into capillaries with LED power 20% and MST power 40%; each sample was scanned three times. The MO.Affinity Analysis software fitted binding curves to determine dissociation constants (Kd) and evaluate the binding affinity between small molecules and TrkB protein.

2.4 Animal Behavioral Tests

All behavioral tests were conducted in a calm, softly illuminated environment featuring a light intensity of 10–20 lux, a temperature range of 22–25 °C, and a relative humidity of 50%–60%. Mice were acclimated in the behavioral testing area for a minimum of 30 minutes prior to experimentation. Following each mouse's trial, the apparatus was cleaned with 75% ethanol to prevent olfactory contamination. For the tail suspension test (TST), adhesive tape was firmly attached approximately 1 cm from the tip of the mouse tail. Mice were suspended from a horizontal support with their heads positioned roughly 30 cm above the ground and baffles were arranged on both sides for isolation. The testing lasted for 6 minutes, and the total time spent immobile was measured during the last 4 minutes[67]. Immobility was characterized by a lack of active struggling while maintaining a vertically still body posture. For the forced swim test (FST), a transparent cylindrical container with a diameter of 25 cm

and height of 30 cm was filled with water at 25±0.5 °C to a depth of 15 cm to ensure that hind limbs could not touch the bottom[67]. Mice underwent a 1-minute acclimatization period in the water, after which their time spent immobile was noted during the following 5 minutes. Immobility was indicated by only slight limb movements necessary to keep the head above the water without engaged swimming. For the sucrose preference test (SPT), the two-bottle method was used[68]. One bottle contained 1% sucrose solution and the other contained pure water. Bottle positions were swapped every 24 h to eliminate position preference throughout the 48 h habituation period. Prior to testing, food and water were withheld for 24 hours. The volume of consumed sucrose solution and water was measured over a 2-hour period. The sucrose preference rate (%) is calculated as (volume of sucrose consumed / (volume of sucrose consumed + volume of water consumed)) × 100%.

2.5 Histology, Immunofluorescence and Golgi Staining

Tissue perfusion and fixation were performed after mice received deep anesthesia and pre-chilled 0.01 mol/L PBS (pH 7.4) was perfused through the left ventricle at approximately 5 mL/min for 5 min to remove blood. Following this, a 4% paraformaldehyde solution (prepared in 0.1 mol/L PBS, pH 7.4) was perfused at a rate of 3 mL/min for 15 minutes to preserve the brain tissue. The entire brains were then collected and post-fixed in 4% paraformaldehyde at a temperature of 4 °C for a duration of 4 to 6 hours. The tissues underwent a sequential dehydration process in 20% sucrose and then 30% sucrose at 4 °C until they sank. Samples were embedded in OCT compound, frozen at -20 °C, and sectioned to a thickness of 20 μm. The sections were mounted on slides with a positive charge and stored at -80 °C. For the cell coverslip samples, cells were fixed in 4% paraformaldehyde at room temperature for 15 minutes and subsequently washed three times with PBS before proceeding to immunofluorescence staining.

Immunofluorescence staining was performed by thawing tissue sections at room temperature for 30 min followed by three 5-min PBS rinses and permeabilization with 0.1% Triton X-100 in PBS at room temperature for 10 min[69]. Blocking was conducted in a humidified chamber at room temperature for 1 hour with 5% BSA in PBS. Primary antibodies, diluted in 1% BSA-PBS, were then applied and incubated overnight (16–18 hours) at 4 °C

within the humidified environment. The slides underwent three rinses with PBS for 10 minutes each, followed by an incubation with fluorophore-conjugated secondary antibodies at room temperature in the absence of light for 1 to 2 hours. After extensive washing with PBS, nuclei were counterstained for 5 minutes using DAPI, and the slides were mounted with anti-fade medium. Images were captured using a fluorescence microscope with consistent acquisition settings across all groups. Semi-quantification of mean fluorescence intensity was performed utilizing ImageJ software. The target markers analyzed were ZO-1, TUBB3, PNN, and PV.

Golgi-Cox silver staining was performed using the FD Rapid GolgiStain™ kit where intact brains were harvested, protected from light, immersed in 1:1 mixed A/B staining solution with a stain volume no less than 5-fold the brain tissue volume, and incubated at room temperature in the dark for 7–14 days with the staining solution renewed every 2–3 days[70]. Brains were transferred to solution C and incubated at room temperature in the dark for 1–2 days. Gradient ethanol dehydration and xylene clearing were performed. Coronal brain slices of 100 μm thickness were sectioned using a Leica VT1000S vibratome. Silver nitrate development was performed in the dark, and staining intensity was monitored under a microscope. After further dehydration and clearing, sections were mounted with neutral balsam. An Olympus BX53 light microscope was used to select intact hippocampal pyramidal neurons; 5–8 qualified neurons were selected per mouse. The Sholl plugin in ImageJ was used to quantify dendritic arbor complexity and spine density[70].

2.6 Molecular Biological Assays

2.6.1 Protein Extraction

Cell samples underwent three washes using pre-cooled PBS. A volume of 100 to 150 μL of RIPA lysis buffer, which contained protease and phosphatase inhibitors, was applied to each well in 6-well plates. The lysis process took place on ice for 30 minutes, involving brief vortexing for 10 seconds every 5 minutes. For the hippocampal tissue, the ratio of tissue mass (mg) to lysis buffer (μL) was set at 1:10, and the mixture was homogenized using a tissue homogenizer. All samples experienced centrifugation at 12,000 rpm for 15 minutes at a temperature of 4 °C. The supernatant was aspirated with caution to prevent disturbance of the

pellets and lipid layers. Protein concentrations were measured using the BCA assay[71]. Protein samples were adjusted to a consistent concentration, aliquoted, and then stored at −80 °C, ensuring that freeze-thaw cycles did not exceed three times.

2.6.2 JESS Automated Capillary Immunoprotein Quantification

Reagents were prepared on ice according to the ProteinSimple JESS kit instructions[72]. Protein samples were mixed with DTT and Master Mix, denatured at 95 °C for 5 min and immediately chilled on ice. Primary antibodies were diluted in Antibody Diluent II at optimized ratios. Lumino-S substrate and Peroxide were mixed 1:1 freshly before use. All reagents were loaded into the microplate, centrifuged at 2500 rpm for 5 min to remove bubbles, capillaries were inserted, and electrophoresis-chemiluminescence program was run with separation voltage 375 V and separation time 25 min. Compass for SW software was used for analysis with GAPDH as the loading control. Relative expression of target protein = peak area of target protein / peak area of GAPDH.

2.6.3 Single-Cell Transcriptomic Sequencing

Single-cell suspensions were prepared from hippocampus and peripheral blood. Hippocampal tissues were dissected on ice, meninges and blood vessels removed, minced to 0.5 mm^3 fragments, digested with Miltenyi Biotec Neural Tissue Dissociation Kit (Cat.130-107-677) in a 37 °C water bath for 30 min with gentle trituration every 10 min. The reaction was terminated with 0.5% BSA-PBS, filtered through a 40 μm cell strainer. Peripheral anticoagulated blood was diluted with PBS, overlaid onto Ficoll-Paque PLUS separation medium and centrifuged at 400 g for 30 min at room temperature with brake disabled[73]. The mononuclear cell layer was collected and washed twice with PBS. Cell viability ≥85% was verified by trypan blue, and cell concentration was quantified with a Countstar counter.

Cell suspension was adjusted to 300–2000 cells/μL. The SeekOne® DD Single-Cell 3’ mRNA Library Kit (Cytion Bio) coupled with the SeekOne® DD digital droplet system was used for oil-in-water single-cell capture, reverse transcription, cDNA amplification and library construction[74]. Library quality control was performed on an Agilent 4200 TapeStation; qualified cDNA displayed a main peak at 600–2000 bp, and qualified libraries showed a main

peak at 350–750 bp. Libraries were sequenced on an Illumina NovaSeq 6000 platform with PE150 strategy and sequencing depth ≥50 000 reads per cell.

Data analysis was performed using SeekOne® Tools software for raw data quality control, alignment to mm10 reference genome and gene expression quantification. R package Seurat (v4.0) was applied for filtering: nFeature_RNA 200–6 000, mitochondrial gene percentage ≤10%[75]. NormalizeData was used for normalization, and the top 2000 highly variable genes were selected. PCA dimensionality reduction was performed with the first 20 principal components retained. t-SNE non-linear dimensionality reduction and clustering were conducted with resolution set at 0.5–1.2 based on the elbow plot. Cell annotation was assigned based on signature genes. FindAllMarkers (min.pct=0.25, logfc.threshold=0.25) was used to identify marker genes for each cell cluster. FeaturePlot and VlnPlot visualized gene expression, and differences in cell subset proportions between groups were calculated. The clusterProfiler package was used for KEGG pathway enrichment of differentially expressed genes; adjusted $P < 0.05$ was defined as statistically significant enrichment[76]. Pseudotime analysis was performed with Monocle2 (v2.99.3) to construct neutrophil differentiation trajectories based on t-SNE clustering and resolve cell state transitions[77].

2.6.4 Flow Cytometry

Primary cells or dissociated hippocampal single-cell suspensions were adjusted to 1×10^6 cells/mL[78]. One hundred microliters of cell suspension was incubated with corresponding surface fluorophore-conjugated antibodies; single-stain compensation tubes and isotype control tubes were prepared in parallel. Samples were incubated on ice in the dark for 30 min, washed twice with FACS buffer (PBS containing 0.5% BSA and 2 mM EDTA), centrifuged at 400 g for 5 min, resuspended in 200 µL FACS buffer and filtered through a 40 µm strainer. Acquisition was performed on a BD LSRFortessa flow cytometer with at least 10 000 target events collected per tube. FSC-H/FSC-W and SSC-H/SSC-W gating excluded cell aggregates and debris. Data were analyzed using FlowJo v10. This assay was used for primary cell purity validation and quantification of infiltrated neutrophils in the hippocampus.

2.6.5 In Vivo Local Field Potential Recordings in the Hippocampus

Mice were anesthetized with isoflurane (induction 3%, maintenance 1.5%) and fixed in a

stereotaxic frame. The stereotaxic coordinates for the hippocampal DG were bregma −2.0 mm, ±1.5 mm lateral to midline, and −1.5 mm below dura mater. A craniotomy was performed, and tungsten microelectrodes with impedance 0.5–1 MΩ (Plastics One) were implanted and secured with dental cement. Mice recovered for 7 days post-surgery. Recordings were acquired using the Blackrock Cerebus multichannel acquisition system[79]. Signals were amplified 1000-fold, bandpass filtered at 0.5–200 Hz, sampled at 2 kHz. NeuroExplorer software extracted the gamma band (25–55 Hz), and fast Fourier transform (FFT) was applied to compute power spectral density. Power was normalized to the 10 min baseline acquired before behavioral testing, and gamma oscillation power was compared across groups. Electrode placement was verified histologically after experiments.

2.6.6 Peripheral Inflammatory Marker Detection

Approximately 200 μL peripheral blood was collected via retro-orbital sampling, allowed to stand at room temperature for 1 h, and centrifuged at 3000 rpm for 15 min at 4 °C to separate serum, which was aliquoted and stored at −80 °C[80]. Mouse CRP was quantified using the Elabscience ELISA kit (Cat.E-EL-M0670)[81]. EDTA-K_2 anticoagulated whole blood was assayed on the Mindray BC-5180CRP hematology analyzer in pre-dilution mode to obtain absolute neutrophil counts and calculate NLR ratios. Sample measurement was completed within 30 min after collection to avoid hemolysis interference.

2.7 Statistical Analysis

All quantitative data were analyzed using GraphPad Prism 9 and presented as mean ± standard error of the mean (mean±SEM)[82]. Two-group comparisons were performed using independent-sample t-tests. One-way ANOVA was applied for overall comparison among multiple groups; Tukey's post-hoc test was used for pairwise comparisons when the ANOVA yielded significance. Time-series repeated measurements were analyzed by two-way mixed-model repeated-measures ANOVA. The Greenhouse-Geisser correction was adopted when the sphericity assumption was violated. Two-way ANOVA was conducted, and Sidak's multiple-comparisons test was performed at individual time points if a significant interaction was detected. *$p < 0.05$, **$p < 0.01$, ***$p < 0.001$; $p > 0.05$ indicated no statistically significant difference between groups.

3 Results

Prior to formal functional experiments, we validated the purity of isolated primary cells and optimized the experimental conditions for in vitro culture and co-culture systems. Flow cytometry was performed to assess the purification efficiency of multiple primary cell types (Figure S1A–L). Magnetic bead-based purification significantly increased the positive proportions of neutrophils, primary hippocampal neurons, B lymphocytes, astrocytes, T lymphocytes, and microglia (Figure S1B, D, F, H, J, L), yielding high-purity cell populations that met the standards for subsequent in vitro functional assays. We further established and validated an in vitro blood–brain barrier (BBB) model and a non-contact co-culture system of neutrophils and primary hippocampal neurons (Figure S2A–J). The transepithelial electrical resistance (TEER) gradually increased and plateaued over culture duration, indicating stable and successful BBB model construction (Figure S2B). Gradient concentration treatment revealed that high-density neutrophils significantly impaired bEnd.3 cell viability (Figure S2C). Through systematic gradient drug screening, the optimal in vitro working concentrations were determined as 1 μM DOM, 10 μM KET, and 10 μM FLX (Figure S2D–E, G). Moreover, high-concentration neutrophils reduced the viability of co-cultured neurons, whereas DOM, KET, and FLX treatment effectively rescued neutrophil-induced cellular injury (Figure S2H–J). Accordingly, low, medium, and high neutrophil working densities were defined as $5\times10^3/cm^2$, $5\times10^4/cm^2$, and $5\times10^5/cm^2$ to mimic suppressed, homeostatic, and activated neutrophil states, respectively.

Based on the optimized in vitro system, we further constructed and validated three in vivo depression models with distinct neutrophil functional phenotypes, including CRS-induced neutrophil homeostatic model, CRS+LPS-induced neutrophil hyperactivation model, and CRS+anti-LY6G-induced neutrophil suppression model (Figure S3). All three model groups exhibited robust depression-like behaviors, as evidenced by prolonged immobility in the FST and TST and decreased sucrose preference in the SPT compared with control mice. Peripheral inflammatory profiling confirmed distinct inflammatory characteristics among the three models: the CRS+LPS group displayed markedly elevated peripheral NEU counts, NLR, and CRP levels; the CRS group presented moderate

inflammatory indices reflecting neutrophil immune homeostasis; and the CRS+anti-LY6G group showed significantly reduced NEU counts and NLR. The successful modeling rates of the CRS, CRS+LPS, and CRS+anti-LY6G models reached 95%, 63%, and 100%, respectively. Collectively, these results verified the successful establishment of three well-characterized depression mouse models with differential neutrophil functional states, providing reliable in vivo platforms for subsequent pharmacological intervention and mechanistic exploration.

For in vivo MMP9 rescue experiments, stereotaxic AAV injection targeting the hippocampal dentate gyrus (DG) was performed and validated (Figure S4). Briefly, 8-week-old male C57BL/6J mice were acclimatized for 7 days before surgery. On day 0 of the experimental timeline, AAV-MMP9 was stereotaxically delivered into the bilateral hippocampal DG region (Figure S4A–B). EGFP fluorescence derived from the AAV reporter gene was detected on the 14th day post-injection to verify viral transfection efficiency. Representative fluorescence images confirmed robust EGFP expression in the hippocampal DG region, with DAPI staining serving as a nuclear counterstain to delineate the anatomical location Figure S4C). These findings validated the successful and specific transfection of AAV-MMP9 in the hippocampal DG, laying a solid experimental foundation for subsequent in vivo functional rescue assays of MMP9.

3.1 Behavioral alterations and single-cell transcriptomic signatures of hippocampal tissue in mice with LPS-induced acute inflammatory depression model

In order to investigate the cellular and molecular features associated with depression-like behaviors triggered by acute inflammatory stimulation, an acute inflammatory depression model was developed using 8-week-old male C57BL/6J mice through the intraperitoneal administration of LPS (1 mg/kg), while the control group was given an equivalent volume of sterile normal saline. Mice were allowed to acclimate for 7 days before the model was initiated, and a series of behavioral assessments were conducted 10 hours post-drug administration. Findings from the tail suspension test (TST, Figure 1B) and the forced swim test (FST, Figure 1C) indicated a significant increase in immobility time for the LPS group in comparison to the control group; additionally, the sucrose preference test (SPT, Figure 1D) revealed a notable decline in the sucrose preference rate among LPS-treated mice, confirming

that LPS effectively provoked depression-like behaviors[51]. Assessment of peripheral inflammatory markers (Figure 1E–G) indicated that serum CRP levels, the neutrophil-to-lymphocyte ratio (NLR), and counts of peripheral neutrophils (NEU) were significantly higher following LPS treatment compared to the control group, establishing the presence of a systemic inflammatory response.

To delineate the changes in cellular composition of hippocampal tissue under inflammatory conditions, single-cell RNA sequencing (scRNA-seq) was performed on mouse hippocampal samples. After cell annotation, multiple cell populations were identified, including neutrophils, monocytes, macrophages, astrocytes, microglia, and neurons (Figure 1H–I). Comparison of t-SNE clustering profiles and the proportions of cell subpopulations between the CT and LPS groups (Figure 1J–K) revealed obvious differences in hippocampal cellular distribution. Following LPS modeling, the proportion of infiltrated neutrophils in the hippocampus was significantly higher than that in the control group, suggesting that LPS promotes the infiltration of peripheral neutrophils into the hippocampus under inflammatory depression. t-SNE visualization and quantitative analysis of MMP9 gene expression (Figure 1L–M) showed that MMP9 was barely expressed in intrinsic hippocampal cells and was predominantly derived from peripheral neutrophils infiltrating the hippocampus; moreover, LPS treatment markedly upregulated MMP9 expression in infiltrated neutrophils. Collectively, these findings indicate that peripheral neutrophils infiltrating the hippocampus serve as the major cellular source of MMP9 in the LPS-induced acute inflammatory depression model[34].

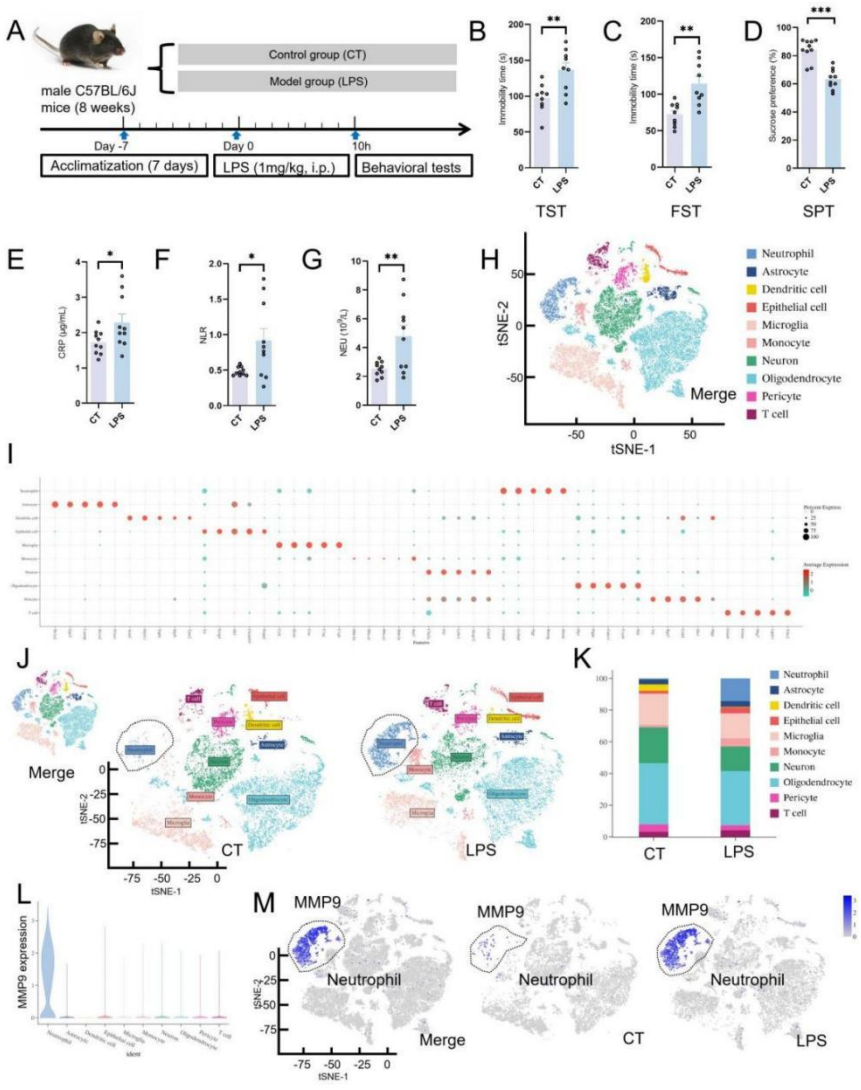


Figure 1. Behavioral assessment and hippocampal single-cell transcriptomic analysis in mice with LPS-induced acute inflammatory depression model

(A) Schematic timeline for establishing the LPS-induced acute inflammatory depression model. Eight-week-old male C57BL/6J mice were acclimatized for 7 days, followed by intraperitoneal injection of LPS (1 mg/kg). Behavioral tests and tissue collection were performed 10 h after LPS administration. (B-D) Measurements of depression-like behaviors in mice. (B) Immobility time in the tail suspension test (TST) (n=10). (C) Immobility time in the forced swim test (FST). (D) Sucrose preference ratio in the sucrose preference test (SPT) (n=10). Mice in the LPS group exhibited significantly prolonged immobility time and reduced sucrose preference, confirming successful establishment of the depression-like model. (E-G) Detection of peripheral inflammatory markers. (E) Serum CRP levels (n=10). (F)

Neutrophil-to-lymphocyte ratio (NLR) (n=10). (G) Peripheral neutrophil count (NEU) (n=10). Elevated peripheral inflammatory indices were observed after LPS challenge, indicating the induction of a systemic inflammatory response. (H-I) t-SNE clustering and cell annotation of single-cell transcriptomes from hippocampal tissue. (H) Global t-SNE clustering plot of hippocampal single cells. (I) Annotation of cell subsets, including neutrophils, monocytes, macrophages, astrocytes, microglia, neurons and other cell populations. (J-K) t-SNE projections and proportional statistics of hippocampal cell subsets in the CT and LPS groups. (J) t-SNE plots showing a marked increase in the proportion of infiltrated hippocampal neutrophils after LPS modeling. (K) Quantitative bar graph verifying the elevated fraction of hippocampal-infiltrating neutrophils upon LPS treatment. (L-M) t-SNE visualization and quantitative expression of the MMP9 gene across cell subsets. (L) t-SNE visualization showing that MMP9 is predominantly enriched in hippocampal-infiltrating neutrophils, while resident hippocampal cells barely express MMP9. (M) Gene expression quantification demonstrating significantly upregulated MMP9 expression in infiltrating neutrophils from the LPS group. Statistical analysis: Unpaired two-tailed t-test was used for intergroup comparisons in panels B – G. Data are presented as mean ± SEM. *$p < 0.05$, **$p < 0.01$, ***$p < 0.001$.

3.2 MMP9 is predominantly expressed in peripheral neutrophils

To validate the findings from single-cell transcriptomics, multiple primary mouse cells were isolated, and protein-level verification was conducted using JESS capillary protein electrophoresis (Figure 2A, D). The results showed that MMP9 protein was highly expressed exclusively in neutrophils, whereas almost no MMP9 protein signal was detectable in neurons, astrocytes, microglia, B cells, and T cells. Primary neutrophils were stimulated in vitro with rapid-acting antidepressants DOM, KET, and FLX for 2 h. Protein electrophoresis and quantitative analysis (Figure 2B, E) demonstrated that DOM and KET significantly increased MMP9 protein expression in neutrophils relative to the CT group, while FLX treatment resulted in lower MMP9 levels compared with DOM and KET groups. Protein detection in hippocampal tissue from mice under physiological conditions (Figure 2C, F) confirmed the presence of MMP9 protein in the hippocampus at baseline, implying that MMP9 can enter the

central hippocampus under physiological states[30]. Further interventions with DOM, KET, and FLX were applied to neurons, microglia, astrocytes, B cells, and T cells (Figure 2G–K). Regardless of drug stimulation, these central and immune cells exhibited negligible MMP9 expression with no significant intergroup differences.

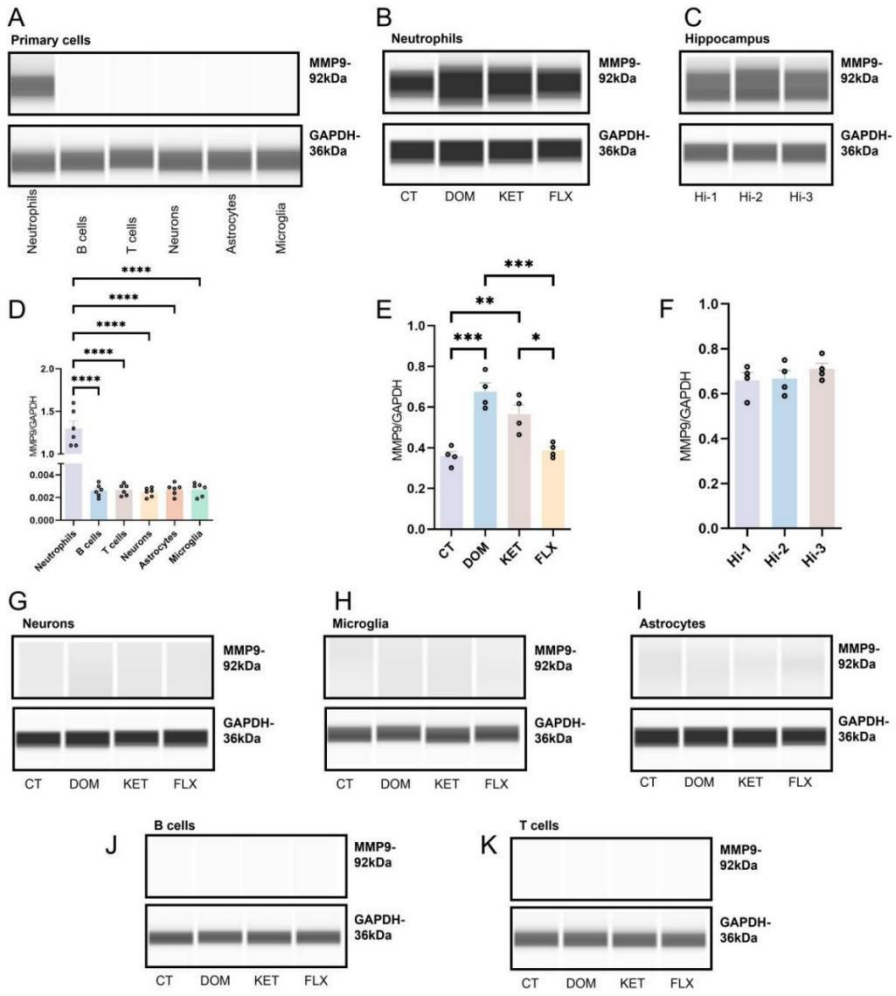


Figure 2. MMP9 protein is predominantly expressed in peripheral neutrophils

(A, D) JESS capillary protein electrophoresis and quantitative analysis of MMP9/GAPDH in multiple primary mouse cell types (n=6). The examined cell populations included neutrophils, B cells, T cells, neurons, astrocytes, and microglia. Neutrophils exhibited markedly higher MMP9 protein abundance relative to all other cell types. (B, E) JESS protein electrophoresis and quantification of primary neutrophils after 2 h stimulation with DOM, KET, or FLX (n=4). Compared with the CT group, DOM and KET significantly upregulated MMP9 protein expression, whereas MMP9 levels in the FLX group were lower than those in DOM- and KET-treated groups.

(C, F) MMP9 protein electrophoresis and quantification in hippocampal tissues from naïve mice (Hi-1, Hi-2, Hi-3) (n=4, technical replicates), confirming detectable MMP9 protein in the hippocampus under physiological conditions. (G–K) Neurons, microglia, astrocytes, B cells, and T cells were treated with rapid-acting antidepressants. MMP9 protein was barely detectable in these cell populations regardless of drug intervention. Statistical analysis: Ordinary one-way ANOVA was applied for multiple-group comparisons in panels D–F. Data are presented as mean ± SEM. *$p < 0.05$, **$p < 0.01$, ***$p < 0.001$.

3.3 DOM and KET remodel the transcriptome of peripheral neutrophils, induce N2 polarization and upregulate MMP9

To investigate the regulatory effects of rapid-acting antidepressants on peripheral immune cells, 8-week-old male C57BL/6J mice were divided into four groups: CT, DOM, KET, and FLX. Corresponding drugs were administered intraperitoneally, and behavioral assessments and peripheral blood scRNA-seq were performed 10 h post-injection. In naive, non-depressed mice, DOM and KET significantly reduced immobility time in the TST (Figure 3C) and FST (Figure 3D) relative to the CT group, consistent with an acute antidepressant-like effect[44]. Because these animals had no baseline depression-like phenotype, changes in the sucrose preference test (Figure 3E) reflect acute effects on sucrose intake rather than a reversal of anhedonia. Taken together, these results indicate rapid-onset pharmacological activity rather than therapeutic efficacy in a depression model. Cell annotation of peripheral blood scRNA-seq data identified immune subpopulations including neutrophils, basophils, eosinophils, B/T lymphocytes, monocytes, dendritic cells, and NK cells (Figure 3F–G). t-SNE clustering and cellular proportion statistics (Figure 3H–I) indicated that the percentage of peripheral blood neutrophils increased after DOM or KET treatment. Expression distribution, t-SNE visualization, and quantitative statistics of MMP9 (Figure 3J–M) revealed that MMP9 was almost specifically expressed in peripheral blood neutrophils, with minimal expression in other peripheral blood cell types.

Peripheral neutrophils were further subdivided into four polarized subpopulations: Bend, N0, N1, and N2 (Figure 4A–B), and a dot plot of signature genes was used to display the molecular marker profiles of each subpopulation (Figure 4C). Comparison of t-SNE

clustering of neutrophil subpopulations across the four groups (Figure 4D), combined with pseudotime differentiation trajectories, pseudotime density distribution, subpopulation spatial distribution, and trajectory comparisons among drug-treated groups (Figure 4E–I), demonstrated that DOM and KET drove neutrophil differentiation toward the N2 polarized phenotype and elevated the proportion of the N2 subpopulation relative to the CT group. Combined with gene expression data, these results suggest that DOM and KET upregulate neutrophil MMP9 expression while inducing N2 polarization of neutrophils.

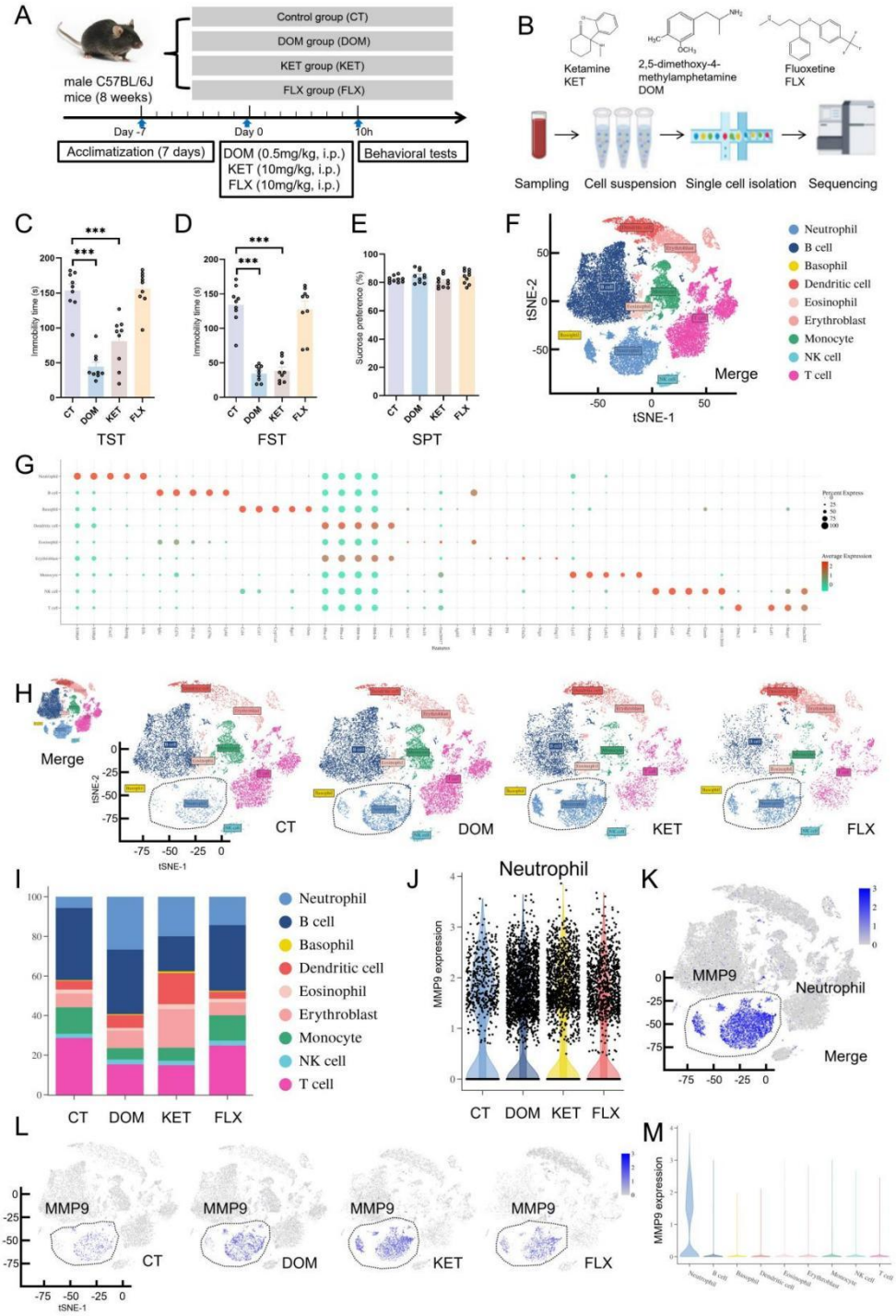


Figure 3. Behavioral assessment and peripheral blood single-cell transcriptomic profiling of mice treated with DOM and KET

(A) Schematic of the animal experimental workflow. Eight-week-old male C57BL/6J mice were acclimatized for 7 days and randomly assigned to four groups: CT, DOM, KET, and FLX. Behavioral tests and peripheral blood single-cell transcriptomic sequencing were conducted 10 h after intraperitoneal drug administration. (B) Experimental workflow for

peripheral blood single-cell sequencing. (C–E) Behavioral results from the TST, FST and SPT (n=10). Treatment with either DOM or KET significantly reduced immobility time in the TST and FST of naïve, non-depressed mice, indicating acute antidepressant-like activity; the SPT here reflects an acute effect on sucrose intake, as these mice had no baseline anhedonia. (F) Global t-SNE clustering plot of peripheral blood single cells. (G) Annotation of immune cell subsets, including neutrophils, basophils, eosinophils, B/T lymphocytes, monocytes, dendritic cells, and NK cells. (H–I) t-SNE projections of peripheral blood cells from the four experimental groups and bar graphs depicting the proportional distribution of each cell subset. The proportion of peripheral neutrophils increased upon DOM and KET treatment. (J–K) Dot plot and t-SNE visualization mapping of MMP9 gene expression within neutrophil subsets. (L–M) Quantitative analysis of MMP9 expression across peripheral blood cell subsets, demonstrating that MMP9 shows nearly neutrophil-restricted expression. Statistical analysis: Ordinary one-way ANOVA was adopted for multiple-group comparisons in panels C–E. Data are presented as mean ± SEM. *$p < 0.05$, **$p < 0.01$, ***$p < 0.001$.

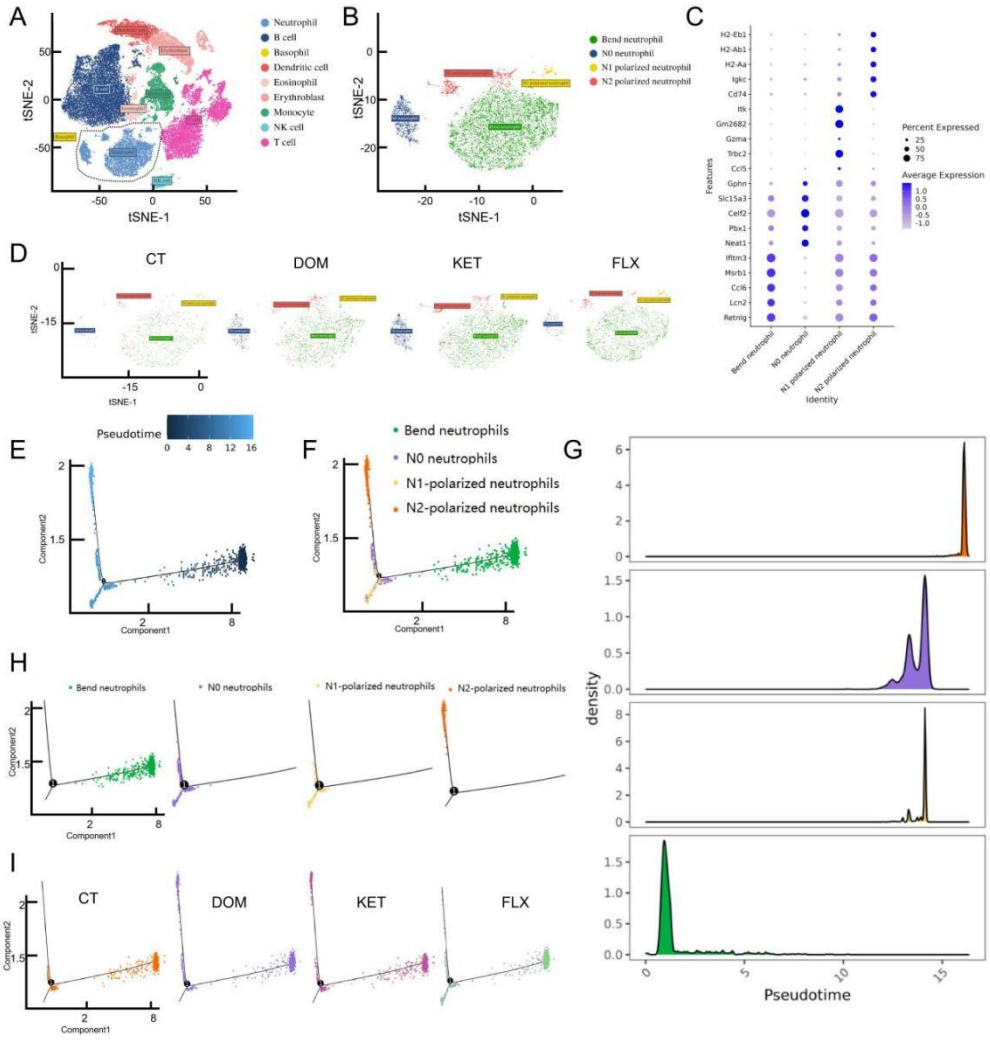


Figure 4. Subclustering and pseudotime trajectory analysis of peripheral blood neutrophil subsets

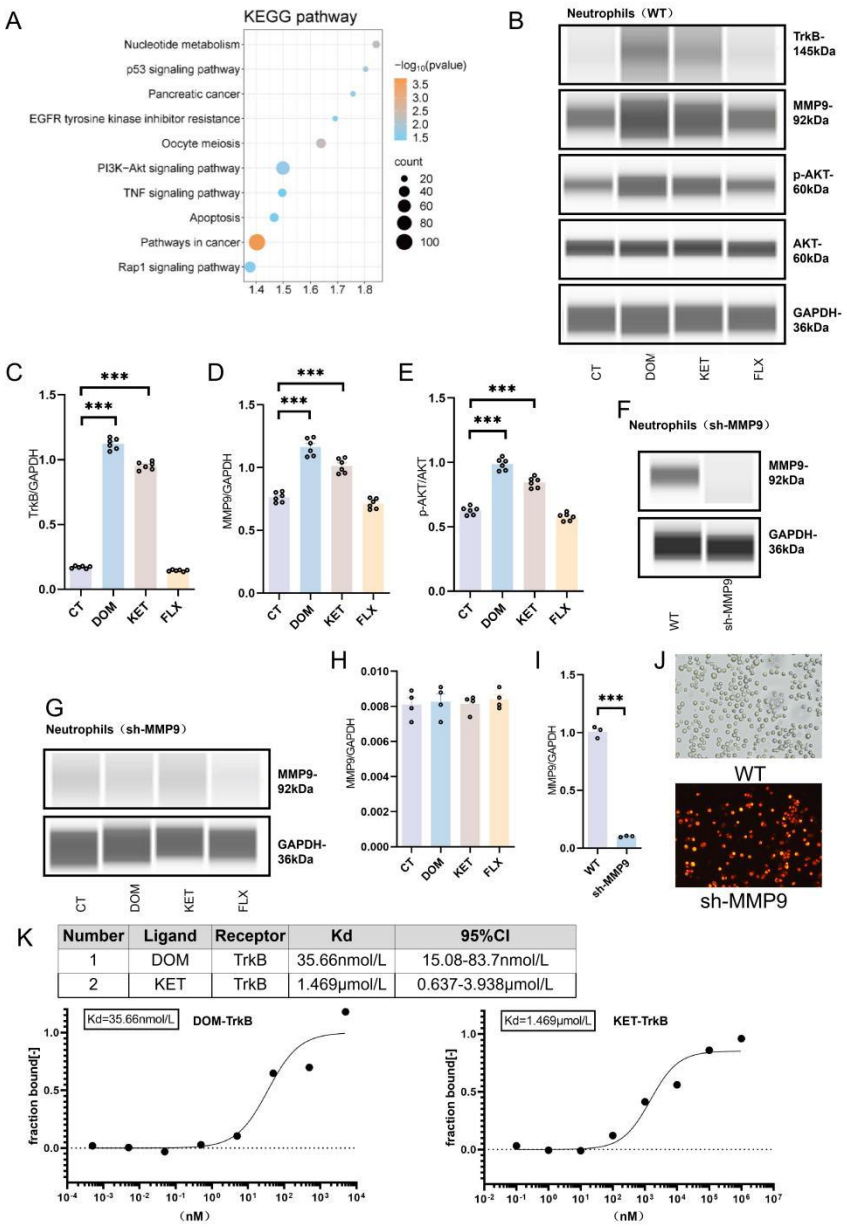
(A) Global t-SNE clustering plot of all immune cells from mouse peripheral blood. (B) Further subclassification of neutrophils into four polarized neutrophil subsets: Bend, N0, N1, and N2. (C) Dot plot showing the expression of signature genes across the four neutrophil subsets, illustrating the expression abundance and cell detection ratio of marker genes in each subset. (D) Comparison of t-SNE projections of neutrophil subsets among the CT, DOM, KET, and FLX groups. (E–F) Pseudotime differentiation trajectories of total neutrophils and their individual subsets. (G) Pseudotime density distribution plot. (H) Spatial distribution of the four neutrophil subsets along the pseudotime trajectory. (I) Comparison of neutrophil pseudotime trajectories across different drug treatment groups. KET and DOM drive neutrophil differentiation toward the N2 polarization state, accompanied by a marked increase

in the proportion of N2 subset cells.

3.4 DOM and KET regulate MMP9 expression in neutrophils

KEGG pathway enrichment analysis was performed on the gene set commonly up-regulated by DOM and KET (Figure 5A). Enrichment results suggested that the TrkB-mediated PI3K-Akt signaling pathway is involved in the regulation of MMP9 expression. Wild-type (WT) primary neutrophils were treated with CT, DOM, KET, and FLX, respectively. Capillary immunoassay and quantitative analysis (Figure 5B-E) showed that compared with the CT group, DOM and KET increased the protein levels of TrkB and MMP9 and elevated AKT phosphorylation (p-AKT/AKT). Such activating effects were absent in the FLX group, which showed no statistically significant difference relative to the CT group.

Neutrophils were transfected with sh-MMP9 plasmid to knock down MMP9. Protein quantification (Figure 5F, I) revealed substantial reduction of MMP9 expression after knockdown, and fluorescence imaging confirmed the transfection efficiency of sh-MMP9 (Figure 5J). Subsequent drug interventions were performed in MMP9-knockdown neutrophils (Figure 5G-H). No significant differences in MMP9 abundance were observed among CT, DOM, KET, and FLX groups under MMP9-knockdown background. Microscale thermophoresis (MST) assay (Figure 5K) yielded dissociation constants Kd = 35.66 nmol/L for DOM-TrkB and Kd = 1.469 μmol/L for KET-TrkB, suggesting the potential direct binding of DOM and KET to the TrkB receptor. Integrating these observations together with recent published evidence[83], we propose that DOM and KET may directly bind TrkB, stabilize TrkB protein conformation, and indirectly potentiate BDNF-triggered downstream PI3K-Akt signaling, thereby up-regulating MMP9 protein expression in neutrophils.



Number	Ligand	Receptor	Kd	95%CI
1	DOM	TrkB	35.66nmol/L	15.08-83.7nmol/L
2	KET	TrkB	1.469μmol/L	0.637-3.938μmol/L

Figure 5. DOM and KET regulate MMP9 expression in neutrophils via the PI3K–Akt pathway

(A) Bubble plot of KEGG enrichment analysis for genes co-upregulated by DOM and KET, indicating that the TrkB-mediated PI3K–Akt signaling pathway participates in the regulation of MMP9 expression. (B–E) JESS capillary protein electrophoresis and quantitative analysis of TrkB, MMP9 and p-AKT/AKT in WT primary neutrophils treated with CT, DOM, KET and FLX (n=6). DOM and KET increased the protein levels of TrkB and MMP9 and promoted AKT phosphorylation, while the FLX group exhibited no significant difference relative to the CT group. (F, I) Protein electrophoresis and quantification of

sh-MMP9-knockdown neutrophils (n=3); (J) Fluorescence imaging verifying the transfection efficiency of the sh-MMP9 plasmid. (G–H) MMP9-knockdown neutrophils with drug intervention (n=4). (K) Microscale thermophoresis (MST) assay for molecular interaction. The dissociation constant Kd of DOM–TrkB was 35.66 nmol/L, and the Kd of KET–TrkB was 1.469 μmol/L, demonstrating that both small molecules directly bind to the TrkB receptor. Multiple-group comparisons in panels C–E, H were performed using ordinary one-way ANOVA; two-group comparisons in panels I were conducted with unpaired two-tailed t-test. Data are presented as mean±SEM, *$p < 0.05$, **$p < 0.01$, ***$p < 0.001$.

3.5 Single administration of DOM or KET does not induce neutrophil infiltration into the hippocampus

Mice were assigned to CT, LPS, DOM, KET, and FLX groups. Behavioral performance, peripheral inflammatory levels, and hippocampal neutrophil infiltration were detected 10 h after intraperitoneal drug injection. Behavioral results from TST (Figure 6C), FST (Figure 6D), and SPT (Figure 6E) showed that LPS induced depression-like behaviors. Peripheral inflammatory markers (Figure 6F–I) demonstrated that serum CRP, NLR, and peripheral NEU counts were markedly elevated after LPS treatment; these peripheral inflammatory indicators showed no obvious increase in groups receiving DOM, KET, or FLX alone. Flow cytometric detection of $CD11b^{+}LY6G^{+}$ neutrophils in hippocampal tissue (Figure 6B, I) revealed that the proportion of hippocampal infiltrated neutrophils was significantly higher in the LPS group than in the control group, while the CT, DOM, KET, and FLX groups exhibited extremely low levels of hippocampal neutrophil infiltration with no intergroup statistical difference. These findings indicate that DOM and KET themselves do not trigger neutrophil recruitment into the hippocampus, and under neutrophil homeostasis, MMP9 can enter the central nervous system independent of neutrophil brain infiltration.

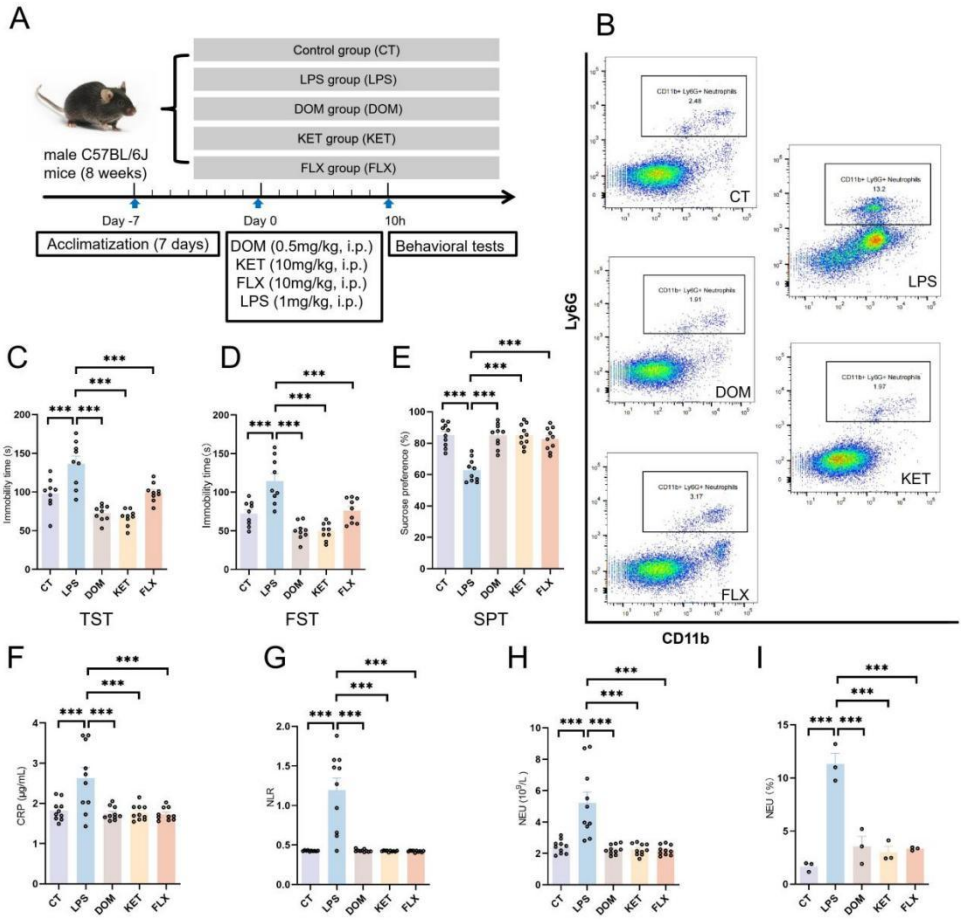


Figure 6. Single administration of DOM or KET does not induce neutrophil infiltration into the hippocampus

(A) Schematic diagram of animal experimental workflow. Mice were divided into CT, LPS, DOM, KET and FLX groups. Behavioral assessments, peripheral inflammatory level detection and hippocampal neutrophil infiltration analysis were performed at 10 h after intraperitoneal administration. (B,I) Flow cytometry dot plots and quantitative statistics of $CD11b^{+}Ly6G^{+}$ neutrophils in the hippocampus; the level of hippocampal neutrophil infiltration was significantly elevated in the LPS group (n=3). The extent of hippocampal neutrophil infiltration remained extremely low in CT, DOM, KET and FLX groups, with no statistically significant differences among these groups, indicating that MMP9 can enter the central nervous system independent of neutrophil brain infiltration under homeostatic conditions. (C–E) Results of TST, FST and SPT behavioral tests (n=10). LPS induced depressive-like behaviors in mice, while DOM, KET and FLX reversed this depressive phenotype. (F--H) Detection of peripheral inflammatory markers (n=10). CRP, NLR and NEU

levels were elevated in the LPS group, whereas following treatment with DOM, KET or FLX, these inflammatory indices showed no statistically significant difference from the CT group. Multiple-group comparisons in panels C–E and F–I were performed using ordinary one-way ANOVA. Data are presented as mean±SEM, *$p < 0.05$, **$p < 0.01$, ***$p < 0.001$.

3.6 MMP9 crosses the in vitro blood–brain barrier independent of neutrophil transendothelial migration

Three neutrophil seeding densities (low, medium, high) were set to mimic suppressed, homeostatic, and activated neutrophil states, respectively, followed by co-culture with an in vitro blood–brain barrier (BBB) model. The high-density (activated neutrophil) group exhibited substantially decreased TEER, increased barrier permeability, a greater number of neutrophils undergoing transendothelial migration, and higher MMP9 concentrations in the lower-chamber supernatant compared with the low- and medium-density groups. In contrast, TEER and barrier permeability in medium- and low-density neutrophil groups were not statistically different from the control group, and these conditions did not disrupt the structural integrity of the BBB (Figure 7B–E).

Medium-density neutrophils representing the homeostatic state were selected for drug intervention experiments, including short-term (1 h) and long-term (48 h) drug treatments (Figure 7F). After 48 h of DOM or KET treatment, BBB TEER decreased, permeability increased, and the number of neutrophils migrating to the lower chamber was markedly elevated (Figure 7G–H, J). Under 1 h short-term drug treatment, neutrophil migration to the lower chamber was undetectable, yet MMP9 protein concentration in the lower-chamber medium was significantly higher than that in the control group (Figure 7I). This result demonstrates that MMP9 protein can cross the in vitro BBB directly, independent of neutrophil transendothelial migration.

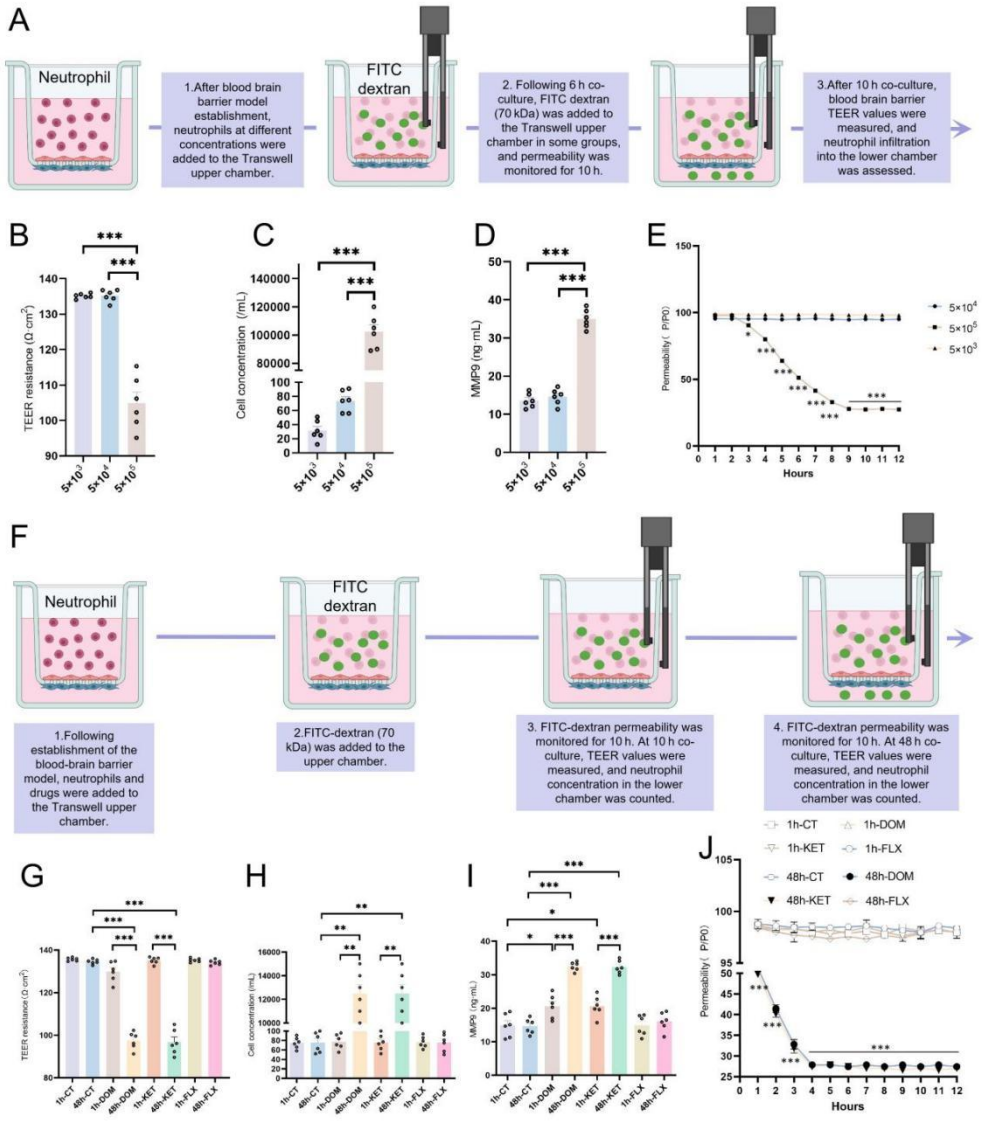


Figure 7. MMP9 crosses the in vitro blood-brain barrier independent of neutrophil transendothelial migration

(A) Schematic diagram of the Transwell in vitro blood-brain barrier (BBB) model. Three neutrophil concentrations (low, medium and high) were set to mimic suppressed, homeostatic and activated neutrophil states, respectively. (B–E) Assessment of BBB function after co-culture with neutrophils at different concentrations; (B) Measurement of TEER values (n=6); (C) Count of neutrophils undergoing transendothelial migration (n=6); (D) MMP9 protein concentration in the lower chamber medium (n=6); (E) Detection of BBB permeability (n=5). High-concentration (activated) neutrophils markedly disrupted barrier function, whereas medium- and low-concentration groups showed no significant differences compared with the control group. (F) Schematic workflow of the Transwell in vitro BBB

model. After BBB model establishment, neutrophils and test drugs were added to the upper chamber. 70 kDa FITC-dextran was supplemented in the upper chamber. Transendothelial electrical resistance (TEER) was detected at 10 h and 48 h of co-culture, the number of neutrophils migrated to the lower chamber was quantified, and the transmembrane leakage of FITC-dextran was monitored simultaneously. (G) TEER measurements of the BBB model under different treatment conditions (n=6). (H) Count of infiltrated neutrophils in the lower Transwell chamber (n=6). (I) Detection of MMP9 protein concentration in the lower chamber across different treatment groups (n=6). (J) Dynamic BBB permeability evaluated using 70 kDa FITC-dextran; P/P0 denotes relative permeability (n=5). CT, control group; DOM, DOM-treated group; KET, ketamine-treated group; FLX, fluoxetine-treated group. 1 h and 48 h represent 1 h and 48 h of drug treatment, respectively. Multiple-group comparisons in panels B–D and G–I were performed using ordinary one-way ANOVA; panels E and J were analyzed by two-way mixed-model repeated-measures ANOVA to test the interaction effect between treatment and time. Data are presented as mean±SEM, $*p < 0.05$, $**p < 0.01$, $***p < 0.001$.

3.7 Transient small-molecule permeabilization of the blood–brain barrier induced by short-term DOM and KET treatment depends on MMP9

Wild-type (WT) and sh-MMP9-modified neutrophils were co-cultured with the blood-brain barrier model, followed by continuous dynamic monitoring for 10 h (Figure 8A). In the WT-neutrophil co-culture system, short-term DOM and KET treatment did not alter TEER or macromolecular permeability; only transient elevation of small-molecule permeability was observed within the 8-h time window (Figure 8B, C, D). After MMP9 was silenced in neutrophils, this transient small-molecule permeabilization effect was completely abolished, and no statistically significant differences were found in all measured parameters at each time-point compared with the CT group (Figure 8E, F, G). These results demonstrate that the transient small-molecule permeabilization of the blood-brain barrier induced by short-term drug exposure depends on neutrophil-derived MMP9 protein expression.

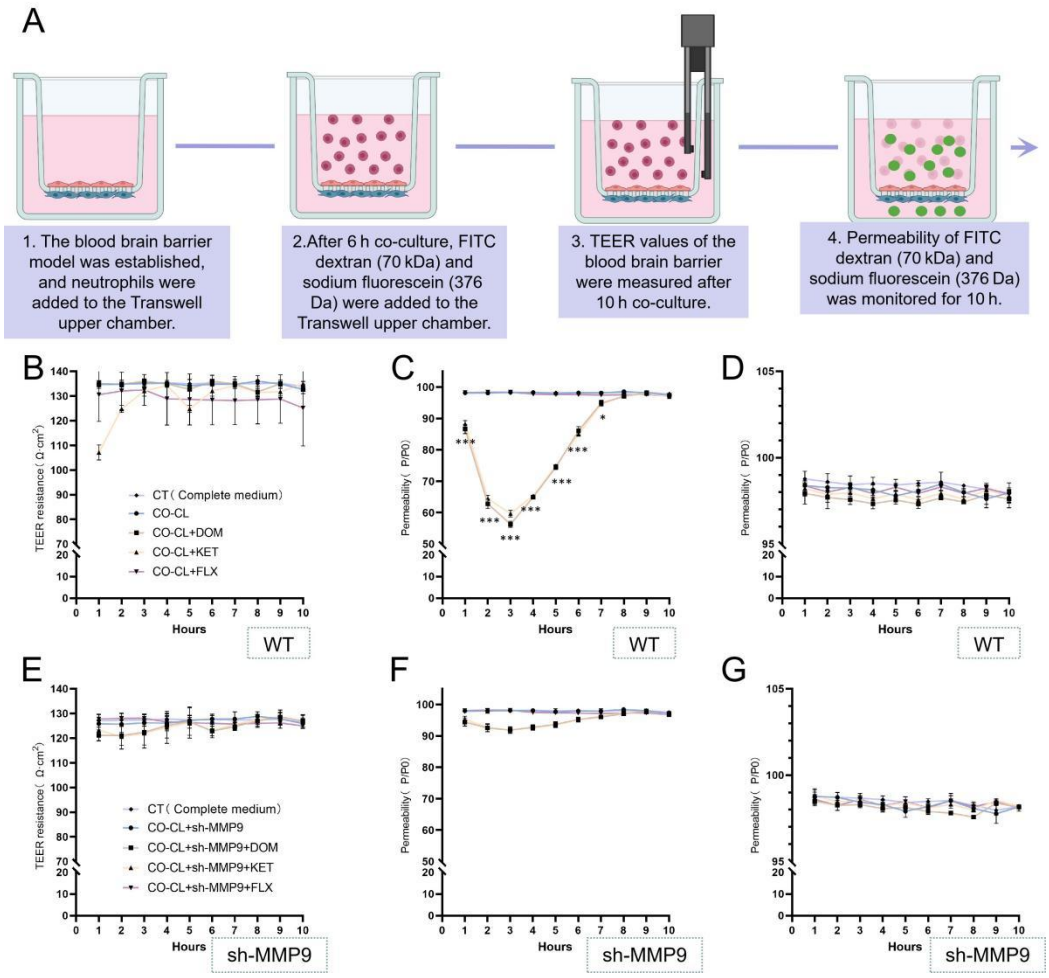


Figure 8. Transient small-molecule permeability of the blood-brain barrier induced by short-term drug treatment depends on MMP9

(A) Schematic diagram of the 10 h dynamic monitoring experiment for the in vitro blood-brain barrier (BBB). Experiments were performed using WT, sh-MMP9 neutrophil systems, respectively. (B-D) WT neutrophil co-culture system. After short-term DOM and KET treatment, TEER and macromolecular permeability remained unchanged throughout the time course relative to the CT group, while transient elevation of small-molecule permeability was observed only within 8 h (n=5). (E-G) sh-MMP9-silenced neutrophil system. The transient small-molecule permeability phenomenon was completely abolished, and no statistically significant differences were found at all time points compared with the CT group (n=5). Panels B–G were analyzed by two-way mixed-model repeated-measures ANOVA to test the interaction effect between treatment and time. Data are presented as mean±SEM, *$p <$ 0.05, **$p < 0.01$, ***$p < 0.001$.

3.8 DOM and KET upregulate Caveolin-1-mediated transcytosis to achieve transient small-molecule permeabilization without disrupting tight junction proteins

To elucidate the molecular mechanism underlying transient permeabilization, bEnd.3 endothelial cell samples were collected at 2 h and 8 h. JESS analysis of tight junction proteins claudin-1, claudin-5, and ZO-1 (Figure 9A–B, D–G) showed no statistically significant differences in claudin-1, claudin-5, or ZO-1 expression between DOM/KET groups and the CT control group at either time point. ZO-1 immunofluorescence staining (Figure 9H–I, K) revealed continuous and intact tight junction structures in endothelial cells across all groups, without protein fragmentation or redistribution, suggesting that the drugs do not open the BBB via degradation of tight junction proteins. Assessment of the transcytosis protein Caveolin-1 at the 8 h time point demonstrated significantly higher Caveolin-1 protein levels in DOM- and KET-treated groups relative to the CT group (Figure 9C, J). Collectively, these data show that under neutrophil homeostasis, short-term DOM and KET stimulation does not disrupt tight junction architecture; instead, it enhances endothelial transcytosis by upregulating Caveolin-1[84], thereby mediating transient small-molecule permeabilization.

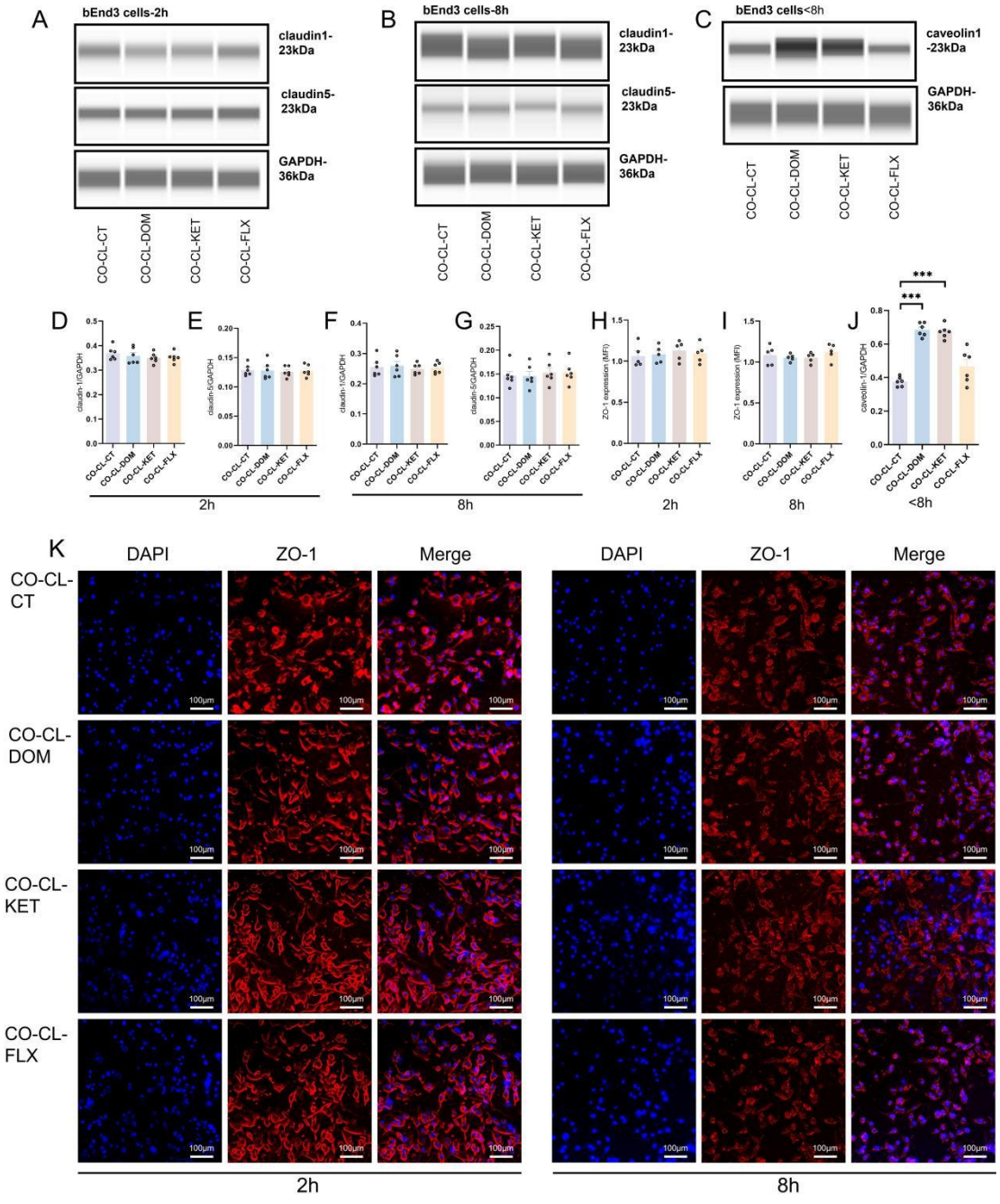


Figure 9. DOM and KET upregulate Caveolin-1-mediated transcytosis without disrupting tight junction proteins

(A–B, D–G) JESS detection of tight junction proteins claudin-1, claudin-5 and ZO-1 in bEnd.3 cells at two time points (2 h and 8 h). No significant differences in the expression levels of tight junction proteins were observed in the DOM and KET groups compared with the CT group (n=6). (H–I, K) Immunofluorescence staining of ZO-1. The tight junction structures of endothelial cells remained continuous and intact in all groups, without protein fragmentation or redistribution (n=5). (C, J) Protein electrophoresis and quantitative analysis

of transcytosis protein Caveolin-1 at the 8 h time point (n=6). DOM and KET treatment markedly upregulated Caveolin-1 protein expression. These results suggest that short-term drug exposure enhances transcytosis by upregulating Caveolin-1 to mediate transient small-molecule permeability, rather than disrupting tight junction structures. Multiple-group comparisons in panels D–J were performed using ordinary one-way ANOVA. Data are presented as mean±SEM, *$p < 0.05$, **$p < 0.01$, ***$p < 0.001$.

3.9 MMP9 mediates the protective effects of DOM and KET on primary hippocampal neurons

Wild-type and sh-MMP9-silenced neutrophils were treated with DOM and KET, respectively. In the co-culture system with wild-type neutrophils, compared with the CT group, DOM and KET treatment up-regulated the expression of BCAN, TUBB3 and BCL-2, down-regulated BAX expression (Figure 10B-F). Increased TUBB3 protein levels were further confirmed by TUBB3 immunofluorescence staining (Figure 10L, N), indicating enhanced neuronal plasticity and suppressed cellular apoptosis. In the co-culture system using sh-MMP9-silenced neutrophils, DOM- and KET-mediated effects including up-regulation of BCAN and TUBB3, down-regulation of BAX were completely abolished. No statistically significant differences were detected between drug-treated groups and the CT group (Figure 10G-K, M, O).

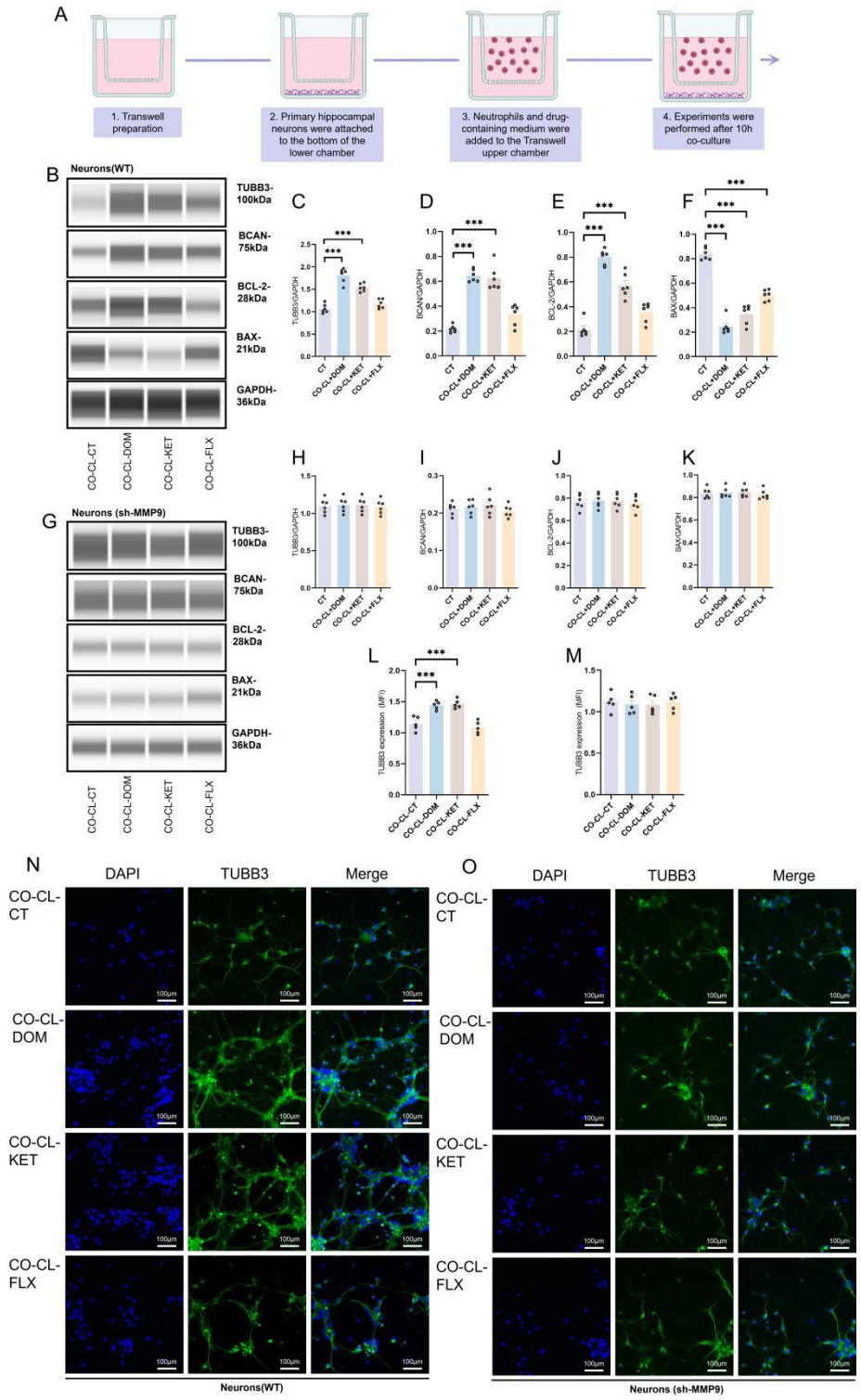


Figure 10. MMP9 mediates the protective effects of DOM and KET on primary hippocampal neurons

(A) Schematic diagram of the Transwell non-contact co-culture system of neutrophils and primary hippocampal neurons. Neutrophils (WT/sh-MMP9) were seeded in the upper chamber, and primary hippocampal neurons were cultured in the lower chamber. (B–F)

Results from the WT neutrophil co-culture system (n=6). DOM and KET upregulated the protein expression of BCAN, TUBB3 and BCL-2, and downregulated BAX expression. (L, N) Immunofluorescence staining of TUBB3 in neurons (n=5). The fluorescence intensity of TUBB3 was increased after DOM and KET treatment. (G–K) sh-MMP9 neutrophil co-culture system. The regulatory effects of DOM and KET on neurons were completely abolished, with no statistical differences between drug-treated groups and the CT group (n=5 or 6). Multiple-group comparisons in panels C–F, H-K, L and M were performed using ordinary one-way ANOVA. Data are presented as mean±SEM, $*p < 0.05$, $**p < 0.01$, $***p < 0.001$.

3.10 Both neutrophil activation and suppression induce depression-like behaviors, and MMP9 serves as a key molecule governing depressive phenotypes

A neutrophil activation animal model was established via intraperitoneal injection of low-dose LPS every other day for 14 days. Groups included CT, LPS, and LPS + MMP9-IN-1. Behavioral tests revealed that mice in the LPS group developed depression-like behaviors compared with the CT group; intervention with the MMP9-IN-1 inhibitor markedly ameliorated depressive phenotypes relative to the LPS group (Figure 11C–E, G). Peripheral inflammatory marker detection (Figure 11I–K) showed that serum CRP, NLR, and NEU levels were significantly elevated in the LPS group versus the CT group; MMP9-IN-1 treatment reduced these inflammatory indicators relative to the LPS group.

A neutrophil suppression model was generated by anti-LY6G administration every other day for 14 days, with groups of CT, anti-LY6G, and anti-LY6G + AAV-MMP9. Mice receiving anti-LY6G also exhibited prominent depression-like behaviors. Local rescue via stereotaxic injection of AAV-MMP9 into the hippocampal DG region significantly reversed these depression-like phenotypes (Figure 11F–H). Peripheral inflammatory markers (Figure 11L–N) demonstrated that peripheral NLR and NEU counts in anti-LY6G and anti-LY6G + AAV-MMP9 groups were markedly lower than those in the CT group, yet behavioral phenotypes were rescued after AAV-MMP9 supplementation. These results indicate that either excessive activation or functional suppression of neutrophils can trigger depression-like behaviors, and MMP9 is a critical molecule regulating depressive phenotypes.

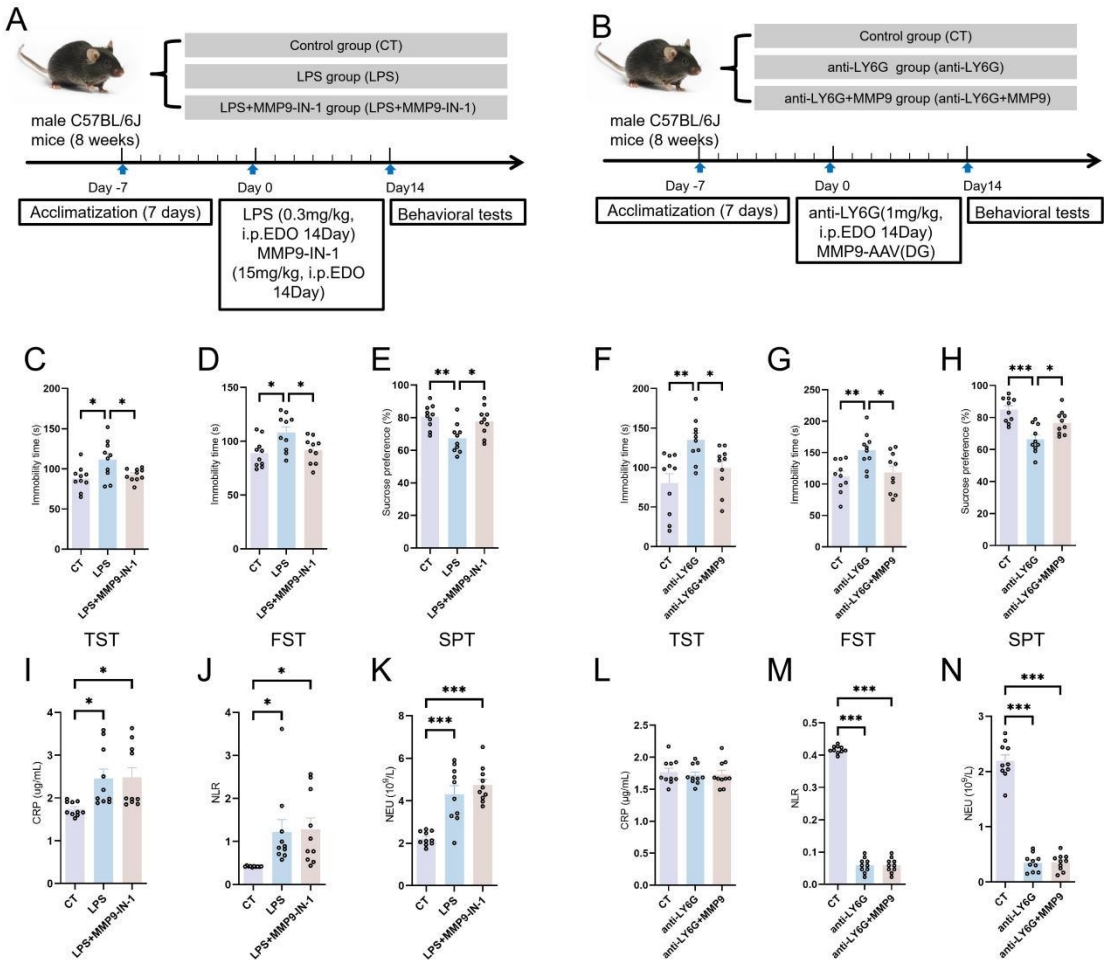


Figure 11. Both activated and suppressed neutrophil states can induce depressive-like behaviors, and MMP9 acts as a key molecule regulating depressive phenotypes

(A) Schematic workflow of animal experiments for the neutrophil activation model (long-term LPS stimulation combined with MMP9-IN-1 intervention). (B) Schematic workflow of animal experiments for the neutrophil suppression model (long-term anti-LY6G-mediated neutrophil depletion combined with hippocampal AAV-MMP9 rescue). (C–E) Behavioral test results of the LPS activation model. Mice in the LPS group exhibited depressive-like behaviors, and intervention with the MMP9-IN-1 inhibitor markedly alleviated the depressive phenotype. (I–K) Detection of peripheral inflammatory indicators (n=10). Levels of CRP, NLR and NEU were elevated in the LPS group; these inflammatory markers decreased after MMP9-IN-1 treatment. (F–H) Behavioral results of the anti-LY6G neutrophil depletion model. Mice in the anti-LY6G group displayed prominent depressive-like behaviors, and hippocampal DG region AAV-MMP9 rescue reversed this

depressive phenotype (n=10). (L–N) Detection of peripheral inflammatory indicators (n=10). NLR and NEU levels were significantly reduced in the anti-LY6G group. The peripheral NLR and NEU levels in the AAV-MMP9 rescue group were comparable to those in the anti-LY6G group, while the behavioral phenotype of mice was improved (n=10). Multiple-group comparisons in panels C–N were performed using ordinary one-way ANOVA. Data are presented as mean±SEM, *$p < 0.05$, **$p < 0.01$, ***$p < 0.001$.

3.11 In the neutrophil homeostatic depression model, DOM and KET exert rapid antidepressant effects by upregulating hippocampal MMP9

A 14-day chronic restraint stress (CRS) paradigm was used to establish a neutrophil homeostatic depression model. Mice with abnormal peripheral neutrophil counts were excluded, and remaining animals were divided into CT, CRS, CRS + DOM, and CRS + KET groups. Behavioral results showed robust depression-like behaviors in the CRS group; DOM and KET intervention significantly alleviated depressive phenotypes compared with the CRS group (Figure 12B–D). Quantitative measurement of hippocampal MMP9 protein showed no significant difference between the CRS and CT groups, whereas DOM and KET treatment markedly increased hippocampal MMP9 expression (Figure 12E–F). Golgi silver staining revealed that the complexity of hippocampal neuronal dendritic arbors and spine density were substantially decreased in the CRS group, and these neuronal plasticity parameters were restored after DOM or KET treatment (Figure 12G–J). PV and PNN immunofluorescence indicated massive PNN deposition in the CRS group; DOM and KET treatment promoted PNN degradation, while neuronal density showed no intergroup statistical difference (Figure 12K–N). Local field potential recording of Gamma (25–55 Hz) oscillations in the hippocampal DG region demonstrated reduced Gamma power in the CRS group, which was significantly rescued by DOM or KET treatment[32] (Figure 12O–P). Collectively, in the neutrophil homeostatic depression model, DOM and KET upregulate hippocampal MMP9, facilitate PNN degradation, restore neuronal plasticity[33], and recover Gamma circuit oscillatory function, thereby mediating rapid antidepressant actions.

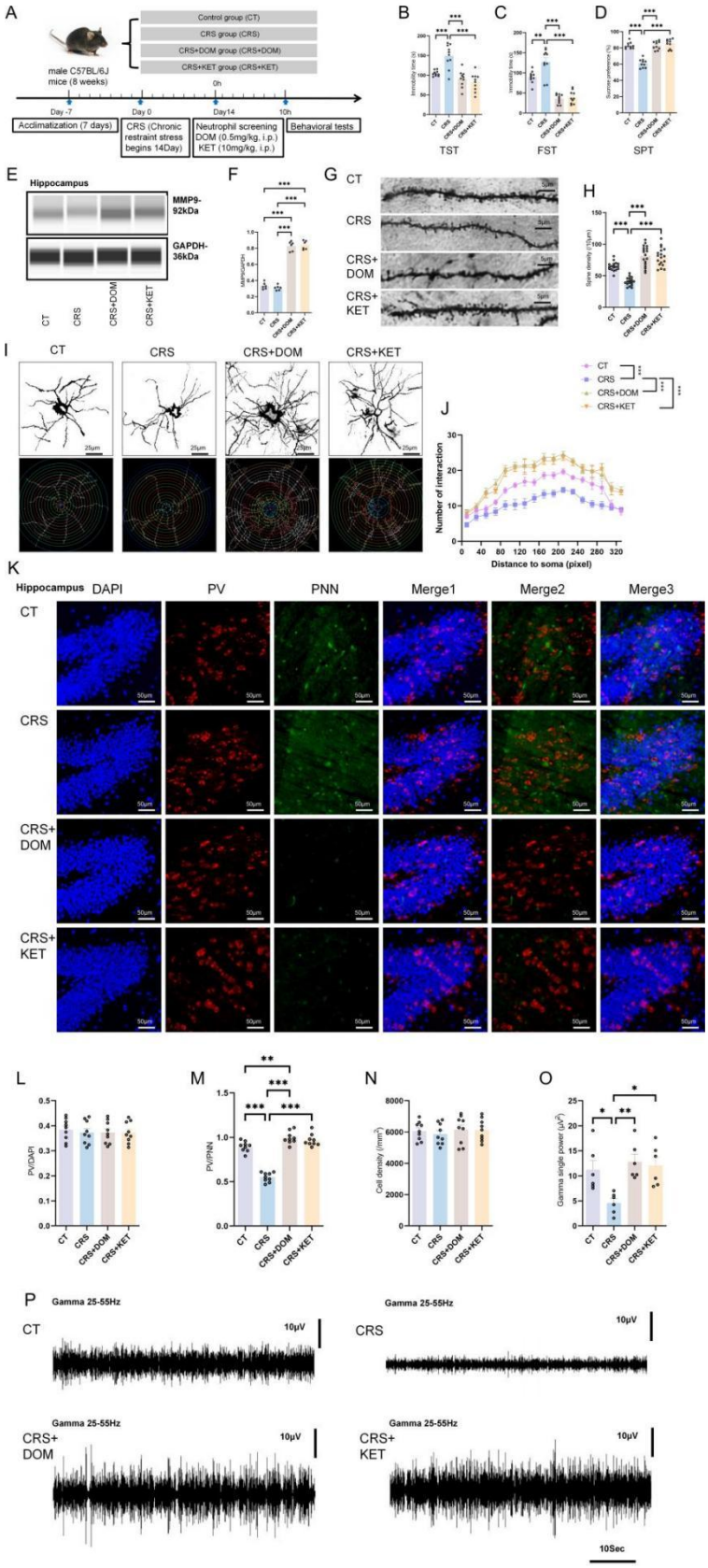


Figure 12. DOM and KET restore neuronal plasticity and circuit function via MMP9 in the CRS neutrophil-homeostasis depression model

(A) Schematic workflow for establishing the CRS (chronic restraint stress) neutrophil-homeostasis depression model. (B–D) Results of TST, FST and SPT behavioral tests (n=10). Mice in the CRS group exhibited robust depressive-like behaviors, and DOM or KET intervention markedly ameliorated the depressive phenotype. (E–F) Quantitative analysis of hippocampal MMP9 protein (n=6). Hippocampal MMP9 expression showed no obvious difference between the CRS and CT groups, while DOM and KET treatment upregulated MMP9 expression. (G–J) Golgi silver staining and quantitative statistics. The complexity of hippocampal neuronal dendritic arborization (n=3, 2 non-overlapping fields per mouse) and dendritic spine density (n=3, 6 non-overlapping fields per mouse) were significantly reduced in the CRS group; these neuronal plasticity-related parameters recovered after DOM and KET treatment. (K–N) Quantitative analysis of PV and PNN immunofluorescence staining (n=3, 3 non-overlapping fields per mouse). Massive PNN deposition was observed in the CRS group; DOM and KET promoted PNN degradation, with no significant differences in neuronal density across groups. (O–P) Local field potential recording of Gamma oscillations (25–55 Hz) in the hippocampal DG region (n=6). Gamma oscillation power was decreased in the CRS group and rescued following DOM and KET administration. Multiple-group comparisons in panels B–D, F, H, L–O and J were performed using ordinary one-way ANOVA. Data are presented as mean±SEM, $*p < 0.05$, $**p < 0.01$, $***p < 0.001$.

3.12 In the neutrophil-suppressed depression model, insufficient peripheral MMP9 supply attenuates DOM and KET efficacy, and MMP9 rescue in the hippocampal DG enhances antidepressant effects

A CRS + anti-LY6G neutrophil-suppressed depression model was constructed, with groups including CT, CRS + anti-LY6G, CRS + anti-LY6G + DOM, CRS + anti-LY6G + KET, CRS + anti-LY6G + DOM + AAV-MMP9, and CRS + anti-LY6G + KET + AAV-MMP9. Hippocampal MMP9 protein detection revealed that hippocampal MMP9 expression was markedly downregulated in the CRS + anti-LY6G group relative to the CT group; DOM or KET monotherapy failed to upregulate hippocampal MMP9, whereas combined treatment with AAV-MMP9 rescue produced significantly higher hippocampal

MMP9 levels than drug monotherapy (Figure 13E–F). Behavioral results showed severe depression-like behaviors in CRS + anti-LY6G mice; DOM or KET alone only partially improved depressive phenotypes, and the therapeutic effect of drugs combined with AAV-MMP9 rescue was superior to monotherapy (Figure 13B–D). Golgi silver staining demonstrated markedly reduced dendritic arbor complexity and spine density in the CRS + anti-LY6G group; monotherapy achieved partial rescue, while combined AAV-MMP9 rescue yielded stronger restoration of neuronal plasticity (Figure 13G–J). PV, PNN immunofluorescence and Gamma oscillation assays showed massive PNN deposition and reduced Gamma power in the CRS + anti-LY6G group. Monotherapy exerted limited effects on PNN degradation and only slightly increased Gamma power; combined AAV-MMP9 rescue robustly promoted PNN degradation and elevated Gamma oscillation power, outperforming monotherapy (Figure 13K–P). These results suggest that when neutrophil function is suppressed, insufficient peripheral MMP9 supply weakens the rapid antidepressant efficacy of DOM and KET, and MMP9 supplementation in the hippocampal DG region improves drug therapeutic outcomes.

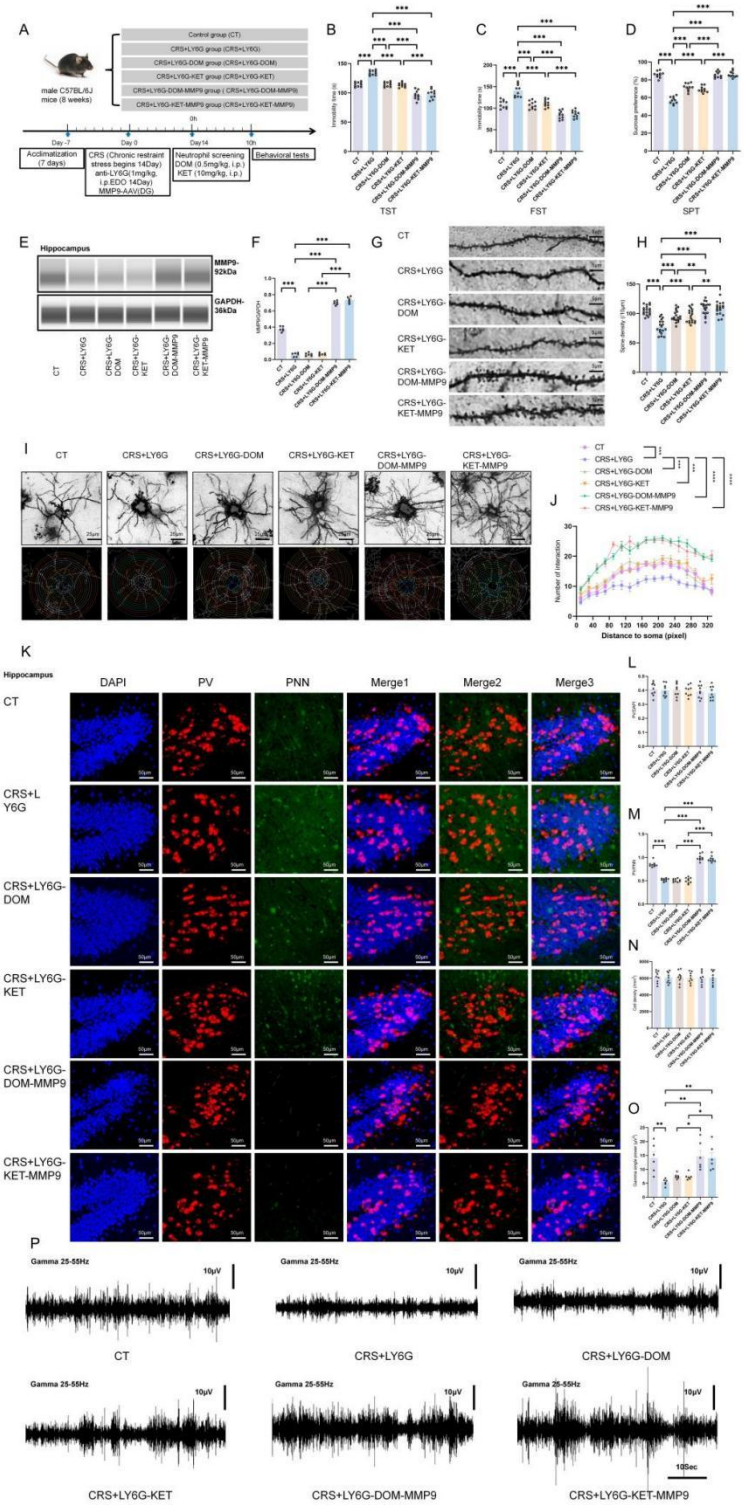


Figure 13. Hippocampal MMP9 rescue enhances the antidepressant efficacy of DOM and KET in the neutrophil-suppressed depression model

(A) Schematic workflow of the CRS+anti-LY6G neutrophil-suppressed depression model. (B–D) Results of TST, FST and SPT behavioral tests (n=10). Mice in the CRS+anti-LY6G group exhibited severe depressive-like behaviors; drug treatment alone only partially

ameliorated the depressive phenotype, whereas combined treatment with drugs and AAV-MMP9 rescue achieved markedly superior therapeutic effects compared with drug monotherapy. (E–F) Quantitative analysis of hippocampal MMP9 protein (n=6). MMP9 expression was significantly downregulated in the CRS+anti-LY6G group; DOM or KET monotherapy failed to upregulate MMP9, and the combined treatment group with AAV-MMP9 rescue showed further elevated MMP9 expression. (G–J) Golgi silver staining and quantitative statistics. Neuronal dendritic arbor complexity (n=3, 2 non-overlapping fields per mouse) and dendritic spine density (n=3, 6 non-overlapping fields per mouse) were markedly reduced in the CRS+anti-LY6G group; drug monotherapy only partially rescued these deficits, while combined AAV-MMP9 rescue produced stronger restorative effects. (K–N) Quantitative analysis of PV and PNN immunofluorescence staining (n=3, 3 non-overlapping fields per mouse). Robust PNN deposition was observed in the CRS+anti-LY6G group; drug monotherapy induced partial improvement, and combined AAV-MMP9 rescue substantially degraded PNN, with no significant differences in neuronal density across all groups. (O–P) Local field potential recording of Gamma oscillations (25–55 Hz) in the hippocampal DG region (n=6). Gamma oscillation power was reduced in the CRS+anti-LY6G group; drug monotherapy yielded partial recovery, whereas combined AAV-MMP9 rescue significantly increased Gamma oscillation power with better outcomes than drug monotherapy. Multiple-group comparisons in panels B–D, F, H, L–O and J were performed using ordinary one-way ANOVA. Data are presented as mean±SEM, $*p < 0.05$, $**p < 0.01$, $***p < 0.001$.

3.13 In the neutrophil-activated depression model, excessive peripheral MMP9 supply impairs the rapid antidepressant effects of DOM and KET

A CRS + LPS neutrophil-activated depression model was established, with groups of CT, CRS + LPS, CRS + LPS + DOM, CRS + LPS + KET, CRS + LPS + DOM + MMP9-IN-1, and CRS + LPS + KET + MMP9-IN-1. Hippocampal MMP9 protein detection showed elevated hippocampal MMP9 expression in the CRS + LPS group relative to the CT group; DOM or KET monotherapy could not alter MMP9 levels in the model group, while co-administration of MMP9-IN-1 inhibitor markedly downregulated hippocampal MMP9

(Figure 14E–F). Behavioral tests revealed severe depression-like behaviors in CRS + LPS mice; DOM or KET monotherapy failed to reverse depressive phenotypes, whereas co-treatment with MMP9-IN-1 significantly augmented the antidepressant effects of the drugs (Figure 14B–D). Golgi silver staining showed that DOM or KET monotherapy could not repair damaged neuronal dendritic arbors or spine density; combined MMP9-IN-1 treatment induced obvious restoration of dendritic architecture (Figure 14G–J). PNN immunofluorescence demonstrated extensive PNN degradation in the CRS + LPS group, with no improvement after DOM or KET monotherapy; co-administration of MMP9-IN-1 restored PNN deposition and alleviated neuronal loss induced by excessive MMP9 (Figure 14K–N). Hippocampal Gamma oscillation recording showed that DOM or KET monotherapy could not increase Gamma power; Gamma oscillation power was significantly recovered upon combined MMP9-IN-1 inhibitor treatment (Figure 14O–P). These findings confirm that excessive peripheral MMP9 supply under neutrophil hyperactivation attenuates the rapid antidepressant effects of DOM and KET.

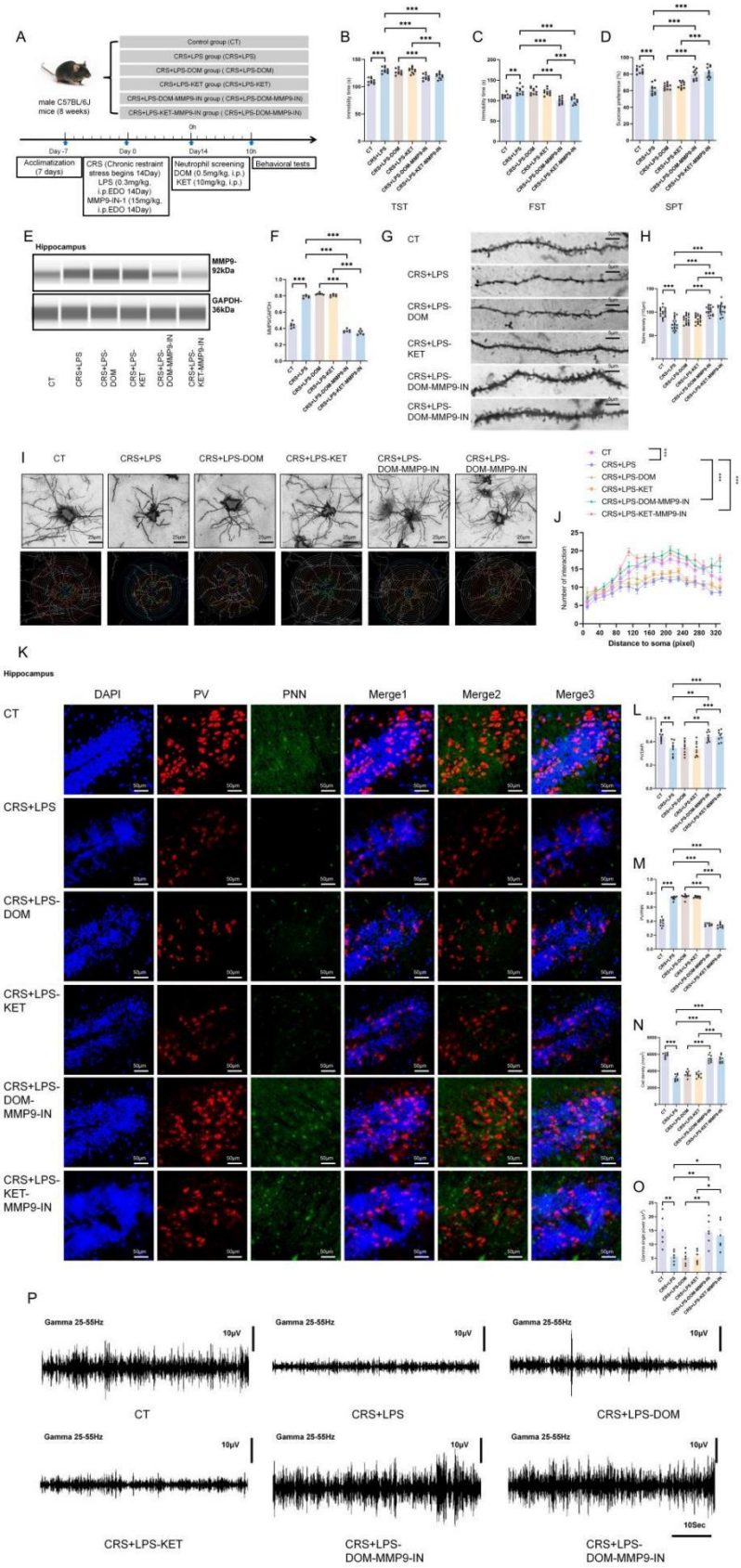


Figure 14. The antidepressant effects of DOM and KET rely on MMP9 function in the neutrophil-activated depression model

(A) Schematic workflow of the CRS+LPS neutrophil-activated depression model. (B, D) Results of TST, FST and SPT behavioral tests (n=10). Mice in the CRS+LPS group exhibited severe depressive-like behaviors; DOM or KET monotherapy failed to reverse the depressive phenotype, whereas combined administration with the MMP9-IN-1 inhibitor markedly potentiated the antidepressant effects, outperforming drug monotherapy. (E–F) Quantitative analysis of hippocampal MMP9 protein (n=6). MMP9 expression was upregulated in the CRS+LPS group relative to the CT group; DOM and KET treatment showed no obvious difference compared with the model group. Blockade of MMP9 function by MMP9-IN-1 significantly reduced MMP9 protein levels. (G–J) Golgi silver staining and quantitative statistics. DOM or KET monotherapy failed to rescue neuronal dendritic arbor complexity (n=3, 2 non-overlapping fields per mouse) and dendritic spine density (n=3, 6 non-overlapping fields per mouse); the neuronal restorative effect was substantially enhanced upon addition of MMP9-IN-1. (K–N) Quantitative analysis of PV and PNN immunofluorescence staining (n=3, 3 non-overlapping fields per mouse). Extensive PNN degradation was observed in the CRS+LPS group, and no difference was detected between drug monotherapy groups and the model group; PNN deposition was restored after combined treatment with MMP9-IN-1. Neuronal density was significantly decreased in the CRS+LPS group; drug monotherapy groups were comparable to the model group, while neuronal density was markedly recovered in the MMP9-IN-1 combined treatment group. (O–P) Local field potential recording of Gamma oscillations (25–55 Hz) in the hippocampal DG region (n=6). Gamma oscillation power was reduced in the CRS+LPS group; no significant difference was found between the drug monotherapy group and the model group, whereas combined MMP9-IN-1 treatment significantly increased Gamma oscillation power with superior effects relative to drug monotherapy. Multiple-group comparisons in panels B–D, F, H, L–O and J were performed using ordinary one-way ANOVA. Data are presented as mean±SEM, $*p < 0.05$, $**p < 0.01$, $***p < 0.001$.

4 Discussion

This study systematically investigated the central scientific question of whether peripherally derived neutrophil MMP9 plays a critical role in rapid antidepressant effects,

integrating single-cell transcriptomic sequencing, primary cell functional assays, an in vitro blood–brain barrier (BBB) model, and multiple animal models of depression. The main findings can be summarized in three respects. First, MMP9 is predominantly expressed by peripheral neutrophils; the rapid-acting antidepressants DOM and KET may directly bind to TrkB and stabilize its conformation at the cell surface, thereby activating PI3K–Akt signaling, driving neutrophil polarization toward the N2 phenotype, and upregulating MMP9 expression. Second, under homeostatic neutrophil conditions, short-term stimulation with DOM or KET does not compromise the tight junctions of the BBB; instead, it upregulates caveolin-1-mediated transcytosis in endothelial cells, enabling MMP9 to cross the BBB and enter the central nervous system, where it subsequently upregulates BCAN and TUBB3, suppresses BAX, and enhances BCL-2 expression, thereby exerting neuroprotective effects on neuronal plasticity. Third, at the in vivo level, MMP9 mediates rapid antidepressant effects through degradation of perineuronal nets (PNNs), improvement of parvalbumin (PV)-positive interneuron circuit function, restoration of dendritic–spine plasticity, and enhancement of gamma oscillation power, and these effects are highly dependent on the functional state of peripheral neutrophils. Collectively, these results demonstrate that MMP9 is an essential molecule for the rapid antidepressant effects of DOM and KET and that drug efficacy is closely linked to the immune state of neutrophils.

4.1 The controversy over the cellular source of MMP9: peripheral neutrophils as the main supplier of central MMP9

The cellular source of MMP9 in the central nervous system has long been a matter of debate. Previous ex vivo studies reported that neurons, microglia, and astrocytes can be induced to express MMP9 under specific inflammatory stimuli[85]. However, single-cell sequencing of the hippocampus in the LPS-induced acute inflammatory depression model, single-cell sequencing of peripheral blood, and JESS-based protein quantification across multiple primary cell types consistently revealed in the present study that, under physiological conditions, MMP9 protein expression in mouse hippocampal neurons, astrocytes, and microglia is extremely low; even upon stimulation with DOM or KET, these resident central cells failed to upregulate MMP9, whereas neutrophils expressed MMP9 abundantly at both

the transcriptional and protein levels. Notably, although MMP9 protein is detectable in hippocampal tissue under physiological conditions, DOM or KET administration alone did not induce massive neutrophil infiltration into the hippocampus, suggesting that, under physiological or homeostatic-depression conditions, hippocampal MMP9 derives mainly from MMP9 secreted by peripheral neutrophils that crosses the BBB, rather than from de novo synthesis by central cells or massive neutrophil brain infiltration. Of course, this study does not entirely exclude the possibility that glial cells are induced to express MMP9 under extreme pathological conditions such as severe brain injury, severe neuroinflammation, or tumorigenesis[86]. In the high-inflammation LPS model used here, large numbers of neutrophils infiltrated the hippocampus, and these infiltrating neutrophils constituted the principal contributors of MMP9. We therefore conclude that the cellular source of MMP9 varies across pathological backgrounds, and that in the neutrophil-homeostatic depression subtype, peripheral neutrophils are the main supplier of central MMP9. This finding also provides an explanation for the contradictory results regarding MMP9 sources in the literature: depending on the inflammatory status of the experimental animals, the predominant cellular source of MMP9 may shift accordingly.

4.2 DOM and KET upregulate neutrophil MMP9 through TrkB-associated signaling

TrkB is the high-affinity receptor for BDNF, and previous studies have focused primarily on the role of neuronal TrkB in the central nervous system in antidepressant action, although the function of TrkB in peripheral immune cells has attracted increasing attention in recent years. It should be noted that the reported detection of TrkB in immune cells has been inconsistent across studies, and most evidence has been derived from transcript-level measurements or from pathological tissues in which cell types cannot be readily distinguished; this inconsistency more likely reflects differences in detection methods and sample contexts rather than a negation of the protein's existence. As terminally differentiated cells, neutrophils have extremely low transcriptional and translational activity, and low or even undetectable Ntrk2 transcripts are therefore not inconsistent with the actual presence of TrkB protein in these cells. Consistent with this notion, multiple lines of evidence suggest that neutrophils are biologically equipped to possess and utilize TrkB protein: TrkB expression has repeatedly

been detected in other myeloid cells such as monocytes/macrophages and dendritic cells[87], which share the myeloid lineage with neutrophils, and neutrophils themselves exhibit functional responses to BDNF, the ligand of TrkB; previous studies have shown that antidepressants can bind TrkB and stabilize its cell-surface conformation, leading to a relative increase in surface TrkB, so that even if endogenous basal expression is low, drug binding itself can drive TrkB enrichment at the cell surface and amplify downstream signaling[83]; in addition, as active phagocytic and endocytic cells, neutrophils may acquire exogenous TrkB protein through endocytic uptake of platelet-derived extracellular vesicles, given that circulating platelets are the principal peripheral reservoir of BDNF[88]and continuously release vesicles carrying membrane protein cargo. Any one of these scenarios, or a combination thereof, is consistent with our experimental observations.

Our results provide evidence supporting the existence of functional TrkB-associated signaling in neutrophils. JESS-based protein quantification directly detected TrkB protein in neutrophils and revealed increased AKT phosphorylation and upregulated MMP9 expression following DOM or KET stimulation, indicating that the TrkB–PI3K–Akt pathway is functionally active in neutrophils. MST assays provided direct physical evidence of the binding affinity of DOM and KET for TrkB, and such receptor binding per se does not depend on high-abundance endogenous expression; these two lines of evidence together form a logically complete chain. Accordingly, regardless of whether the TrkB protein carried by neutrophils originates from low-level endogenous expression, drug-induced enrichment at the cell surface, or uptake of exogenous vesicles, the central functional conclusion of this study—that DOM and KET activate PI3K–Akt and upregulate neutrophil MMP9 through TrkB-associated signaling—remains plausible, and what remains to be clarified in future work are merely details such as the source and abundance of this protein. Pseudotime analysis further revealed that DOM and KET promote neutrophil polarization toward an N2 anti-inflammatory, reparative phenotype, and that N2-polarized neutrophils express higher levels of MMP9. Because N2-like neutrophils are generally considered to participate in tissue repair and remodeling[89], this observation resonates with the role of MMP9 in mediating the restoration of neuroplasticity and further supports the physiological relevance of the above

pathway at the level of cell fate. Consistent with our findings, previous studies have shown that a variety of antidepressants can bind TrkB directly, independent of their classical monoaminergic targets, thereby stabilizing its cell-surface conformation, increasing membrane TrkB abundance, and enhancing its sensitivity to BDNF. As a 5-HT2A receptor agonist and an NMDA receptor antagonist, respectively, DOM and KET likewise exhibit direct affinity for TrkB, suggesting that their rapid onset of action may partly arise from the rapid recruitment and amplification of TrkB signaling in peripheral immune cells: compared with the multi-week neurotransmitter adaptation required for FLX to act through the central serotonin transporter, peripheral myeloid cells are numerous and rapidly turning over, and their membrane receptor conformational changes together with downstream PI3K–Akt pathway activation can be accomplished within minutes to hours—thus matching, on a temporal scale, the antidepressant effects observed within hours of a single administration—rendering this a plausible and important component of their rapid-onset mechanism. Of course, this study cannot exclude the possibility that DOM and KET simultaneously act on neuronal TrkB in the central nervous system and engage other canonical antidepressant pathways. Previous studies have demonstrated that ketamine can disinhibit glutamate release, activate AMPA receptors, and initiate the BDNF–TrkB–mTOR cascade, thereby promoting synaptic protein synthesis and dendritic spine formation[90]; the serotonergic psychedelic class to which DOM belongs can likewise rapidly induce structural plasticity in the prefrontal cortex[44]through 5-HT2A receptor- and TrkB-dependent signaling[91]; in addition, both classes of agents may interact with multiple neurotransmitter systems, including serotonin, dopamine, and glutamate, as well as with neuroinflammatory regulatory pathways. Whether peripheral TrkB-associated signaling acts in parallel with, synergistically amplifies, or forms an upstream–downstream hierarchy with the aforementioned central mechanisms remains to be elucidated and constitutes an important direction for future work.

4.3 The route by which MMP9 crosses the blood–brain barrier: caveolin-1-mediated transcytosis rather than tight junction disruption

The BBB is a critical barrier limiting the entry of peripheral proteins into the central

nervous system. Most previous studies have held that MMP9 compromises barrier integrity by degrading tight junction proteins (claudin-5 and ZO-1), allowing passive leakage of macromolecules into the brain, a process typically accompanied by BBB damage and aggravated inflammation[29]. However, these conclusions were largely derived from models employing high concentrations of MMP9 or prolonged stimulation with activated neutrophils. The present study found that, under homeostatic neutrophil conditions, short-term stimulation with DOM or KET did not downregulate claudin-1, claudin-5, or ZO-1 protein expression, and ZO-1 immunofluorescence revealed no disruption or rearrangement of tight junctions, indicating that no structural damage to tight junctions had occurred. Nevertheless, caveolin-1 expression was upregulated in bEnd.3 endothelial cells, accompanied by a transient increase in the permeability to small-molecule tracers, and this transient permeability was abolished when MMP9 was knocked down. Caveolin-1 is the core protein of caveolae-mediated endocytic vesicles and can mediate the transendothelial transport of macromolecular proteins without causing permanent barrier disruption[84]. Combined with the observation that MMP9 was detectable in the lower chamber 1 h after short-term drug administration without neutrophil migration, we propose that, under homeostatic neutrophil conditions, MMP9 crosses the BBB via caveolin-1-dependent transcytosis rather than through tight junction degradation or cell infiltration. This route enables rapid entry of MMP9 into the brain while avoiding sustained BBB injury, which has important implications for understanding the safety of rapid-acting antidepressants. Admittedly, prolonged high-dose stimulation can still allow high concentrations of MMP9 to disrupt tight junctions, suggesting that MMP9 exerts bidirectional effects and that its levels must be maintained within an appropriate range—a dose dependence that is mutually corroborated with the immune-subtype classification described below.

4.4 MMP9-mediated restoration of neuronal plasticity

Using a non-contact Transwell co-culture system of neurons and neutrophils, under experimental conditions simulating neutrophil homeostasis with short-term rapid-acting antidepressant intervention, this study demonstrated that neutrophil-derived MMP9 regulates the expression of plasticity- and apoptosis-related molecules in hippocampal neurons: it

upregulated the neuronal cytoskeletal protein TUBB3 and BCAN, a core component of perineuronal nets, while downregulating the pro-apoptotic protein BAX and upregulating the anti-apoptotic protein BCL-2, thereby mediating neuroprotection. As a key structural glycoprotein of PNNs, BCAN can be degraded by the proteolytic activity of MMP9, thereby alleviating pathological PNN accumulation[32]and releasing PV-positive interneurons from the functional constraint imposed by PNN structure; PV-positive interneurons are the key cellular population maintaining synchronous discharge of gamma oscillation networks[92], and depressive pathology is frequently accompanied by reduced gamma oscillation power. DOM and KET can restore gamma oscillation function through the MMP9-mediated molecular events described above. In contrast, when neutrophils are overactivated, large numbers of them cross the endothelial barrier and invade the brain parenchyma, releasing a variety of toxic mediators that induce neuronal apoptosis—underscoring neutrophil homeostasis as an essential prerequisite for MMP9 to exert its neuroprotective effects. Meanwhile, the semipermeable membrane of this co-culture system physically separates the two cell populations and permits only the diffusion of soluble secreted proteins across the membrane, thereby excluding, at the experimental-design level, signaling mediated by direct neutrophil–neuron contact and directly demonstrating that the regulation of hippocampal neurons by neutrophils originates from secreted MMP9 rather than from direct cell–cell interaction. Consistently, in the sh-MMP9 gene-silencing experiments, DOM- and KET-mediated neuroprotective phenotypes were completely abolished upon MMP9 silencing, further demonstrating that these neuroprotective effects depend on neutrophil-derived MMP9. Whether this regulation is mediated entirely through the TrkB receptor remains constrained by the aforementioned controversy over the receptor's source and requires orthogonal verification (see Section 4.2).

4.5 Neutrophil-state-based classification of depression subtypes and its therapeutic implications

Based on the multilevel in vitro and in vivo results of this study, the functional state of peripheral neutrophils was identified as a core determinant of the efficacy of the rapid-acting antidepressants DOM and KET. According to the three physiological and pathological states

of neutrophils—homeostatic, activated, and suppressed—depression can be divided into three functional subtypes, each exhibiting markedly distinct drug-response profiles and molecular mechanisms, providing novel experimental evidence and theoretical implications for the precision classification and individualized treatment of depression.

Neutrophil-homeostatic depression (the CRS-only model) is characterized by neutrophil counts and inflammatory indices at normal levels. In this subtype, DOM and KET, through TrkB-associated signaling in neutrophils, drive neutrophil polarization toward the N2 anti-inflammatory subtype and upregulate MMP9 expression; meanwhile, by upregulating caveolin-1-mediated transcytosis in endothelial cells, they achieve central delivery of MMP9 without disrupting BBB tight junctions, leading to degradation of hippocampal PNNs, restoration of neuronal dendritic structure and spine density, suppression of apoptosis, and recovery of gamma oscillation function, ultimately exerting robust and stable antidepressant effects. This subtype defines PI3K–Akt–MMP9 as the core functional hierarchy, with TrkB as the candidate upstream receptor whose source-level confirmation awaits future investigation.

Neutrophil-activated depression (the CRS + LPS model) is characterized by systemic inflammatory activation, peripheral neutrophilia with hippocampal infiltration, and abnormally elevated basal central MMP9 levels. Under these conditions, DOM or KET administration alone failed to repair neuronal damage or ameliorate depressive-like behavior, a finding we attribute to neurotoxicity induced by excessive MMP9, which aggravated neuronal apoptosis and counteracted the protective drug effects; in contrast, co-administration of a specific MMP9 inhibitor restored drug efficacy, suggesting that this subtype reflects MMP9 excess rather than pathway inactivation. This also explains why, in the CRS + LPS model, even with degradation of PNN deposition, drug administration alone failed to enhance gamma oscillations because neuronal apoptosis was not reduced, necessitating co-administration of an MMP9 inhibitor.

Neutrophil-suppressed depression (the CRS + anti-Ly6G model) is characterized by marked peripheral neutrophil depletion and immune hypofunction. The efficacy of DOM and KET was significantly attenuated in this subtype, and the underlying cause is a scarcity of peripheral MMP9 sources, resulting in insufficient hippocampal MMP9 supply to effectively

accomplish PNN degradation and neuronal repair. AAV-MMP9 replenishment in the hippocampal dentate gyrus markedly enhanced drug efficacy, confirming that insufficient peripheral MMP9 supply is the key cause of the low response in this subtype.

In summary, neutrophil MMP9 is a key molecule that bidirectionally regulates depressive phenotypes and drug efficacy, and its expression level and central supply directly determine therapeutic outcome; the antidepressant effects of DOM and KET depend on the neutrophil-associated PI3K–Akt–MMP9 pathway, without inducing neutrophil brain infiltration or compromising BBB integrity. Under homeostatic neutrophil conditions, MMP9 crosses the BBB via caveolin-1-mediated transcytosis, degrades PNNs, and restores neuronal plasticity and gamma oscillation circuit function, thereby mediating rapid antidepressant effects. This neutrophil-state-based classification of depression transcends the limitations of conventional symptom-based classification[93], elucidates—at the level of peripheral immune–central crosstalk—a core mechanism underlying the heterogeneity of depression, and provides important experimental support and theoretical guidance for the clinical precision stratification of depression subtypes and the formulation of individualized rapid antidepressant treatment regimens.

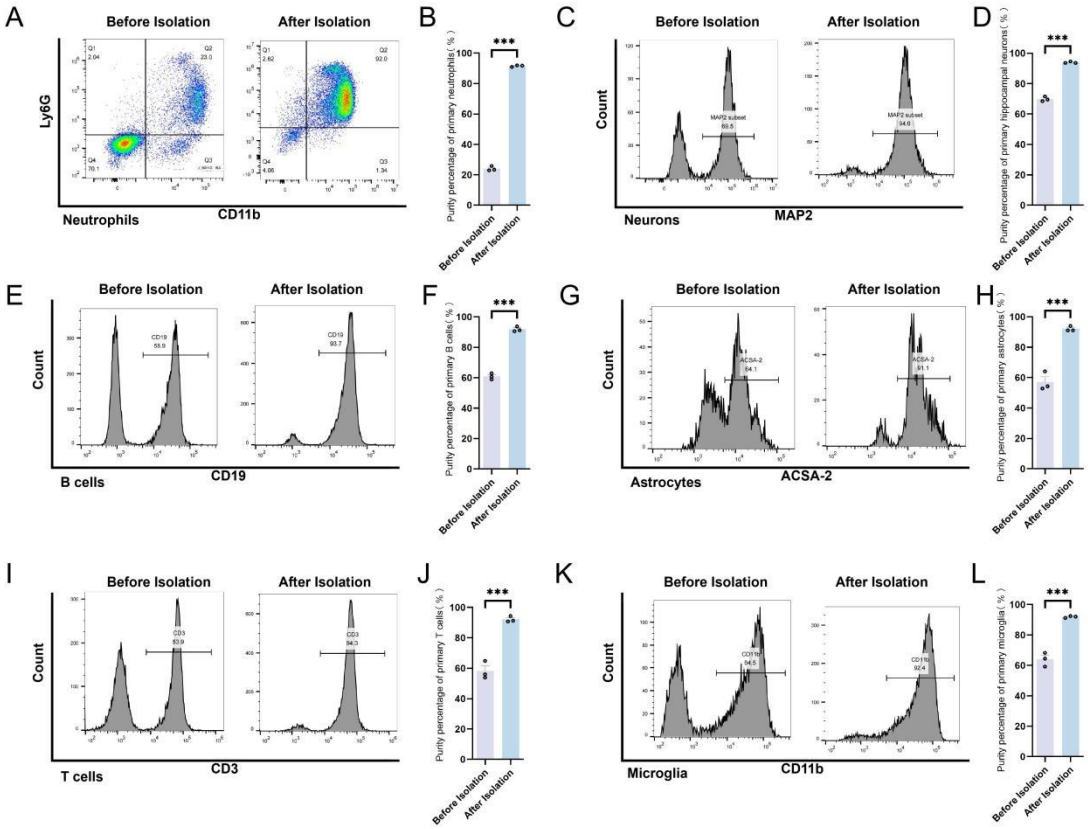


Figure S1. Flow cytometric identification of isolation and purification purity of various primary cells

(A–B) Flow cytometric detection of primary neutrophils labeled with $Ly6G^{+}CD11b^{+}$ (n=3); (A) Flow scatter plots before and after cell isolation; (B) Quantification of cell purity, showing markedly improved neutrophil purity after magnetic bead purification. (C–D) Flow cytometric detection of primary hippocampal neurons labeled with MAP2 (n=3); (C) Flow histograms before and after isolation; (D) Purity quantification, demonstrating significantly increased neuronal purity after purification. (E–F) Flow cytometric detection of B lymphocytes labeled with CD19 (n=3); (E) Flow histograms; (F) Purity quantification, showing elevated B cell purity post purification. (G–H) Flow cytometric detection of astrocytes labeled with ACSA-2 (n=3); (G) Flow histograms; (H) Purity quantification. (I–J) Flow cytometric detection of T lymphocytes labeled with CD3 (n=3); (I) Flow histograms; (J) Purity quantification. (K–L) Flow cytometric detection of microglia labeled with CD11b (n=3); (K) Flow histograms; (L) Purity quantification. These results indicate that the purity of various primary cells obtained via magnetic bead sorting meets the requirements for

subsequent in vitro functional experiments. Multiple-group comparisons in panels B, D, F, H, J and L were performed using ordinary one-way ANOVA. Data are presented as mean±SEM, $*p < 0.05$, $**p < 0.01$, $***p < 0.001$.

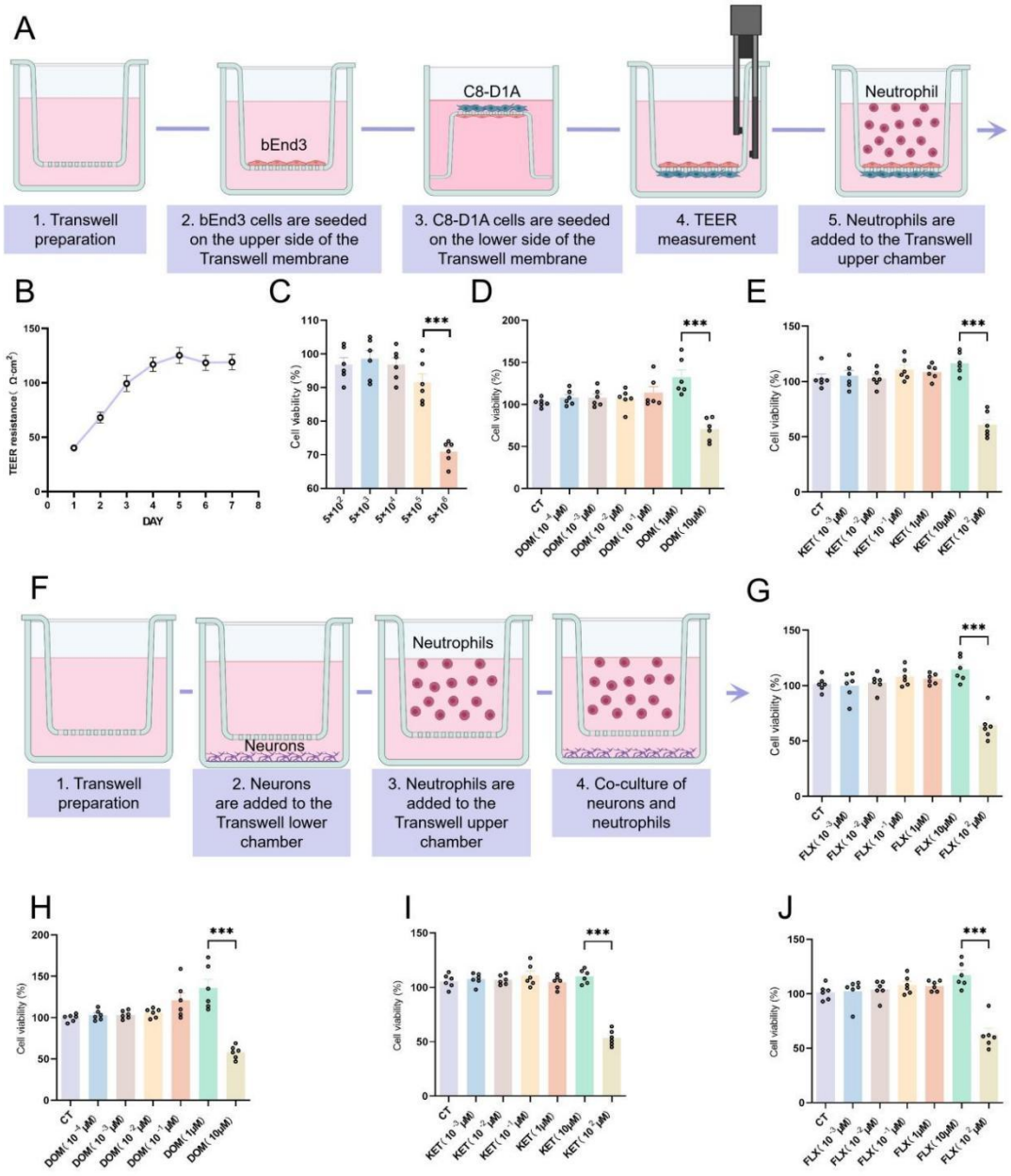


Figure S2. Establishment of in vitro co-culture models and screening of neutrophil and drug concentrations

(A–E) Transwell in vitro blood-brain barrier (BBB) model. (A) Schematic workflow of model construction; C8-D1A astrocytes were seeded in the lower chamber, and bEnd.3 brain microvascular endothelial cells were seeded in the upper chamber. (B) Time course curve of TEER values during culture (n=5). TEER gradually increased and reached a plateau,

indicating successful establishment of the BBB model. (C) Viability assay of bEnd.3 cells incubated with neutrophils at gradient concentrations (n=6). Three working concentrations were selected: $5\times10^3/cm^2$ (low), $5\times10^4/cm^2$ (medium), and $5\times10^5/cm^2$ (high). High-concentration neutrophils markedly reduced endothelial cell viability. (D–E, G) bEnd.3 cells co-cultured with neutrophils under gradient drug treatment (n=6). CCK-8 assay was used to screen the in vitro working drug concentrations: 1 μM for DOM, 10 μM for KET, and 10 μM for FLX. (F) Schematic diagram of the non-contact co-culture model of neutrophils and primary hippocampal neurons. (H–J) Neuronal viability detection after gradient drug treatment (n=6). The in vitro working drug concentrations were determined as 1 μM DOM, 10 μM KET, and 10 μM FLX. Multiple-group comparisons in panels C–E, G and H–J were performed using ordinary one-way ANOVA. Data are presented as mean±SEM, *$p < 0.05$, **$p < 0.01$, ***$p < 0.001$.

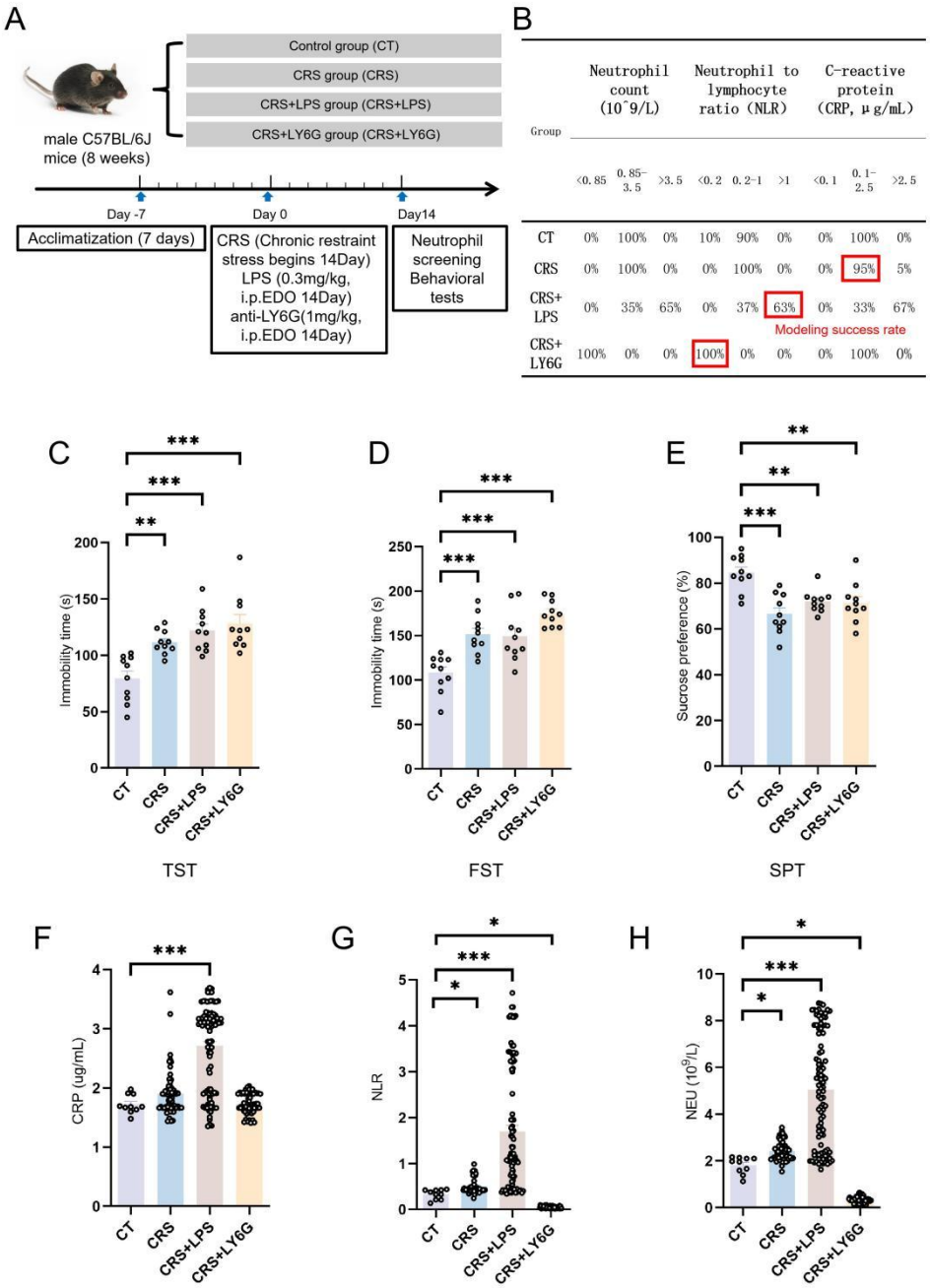


Figure S3. Establishment and validation of three depressive animal models with activated, homeostatic and suppressed neutrophil states

(A) Schematic workflow of animal modeling. Mice were divided into the CT control group, CRS group (neutrophil homeostasis), CRS+LPS group (neutrophil activation), and CRS+anti-Ly6G group (neutrophil suppression). Behavioral tests and peripheral sample collection were performed after 14 consecutive days of intervention. (B) Summary of modeling success rates for depressive models with activated, homeostatic and suppressed neutrophil states. The depression modeling success rates were 95% for CRS (homeostasis), 63%

for CRS+LPS (activation), and 100% for CRS+anti-Ly6G (suppression). (C–D) Immobility time measured by the forced swim test and tail suspension test (n=10). Compared with the CT group, immobility time was significantly prolonged in the CRS group, further increased in the CRS+LPS group, and reached the highest level in the CRS+anti-Ly6G group. (E) Results of the sucrose preference test (n=10). Sucrose preference was markedly reduced in all three model groups relative to the control group. (F–H) Detection of peripheral inflammatory indicators (n=10 or 30); (F) Serum CRP level; (G) NLR ratio; (H) Peripheral neutrophil (NEU) count. These results confirm that three depressive mouse models with distinct functional states of neutrophils were successfully established in this study. Multiple-group comparisons in panels C–H were performed using ordinary one-way ANOVA. Data are presented as mean±SEM, *$p < 0.05$, **$p < 0.01$, ***$p < 0.001$.

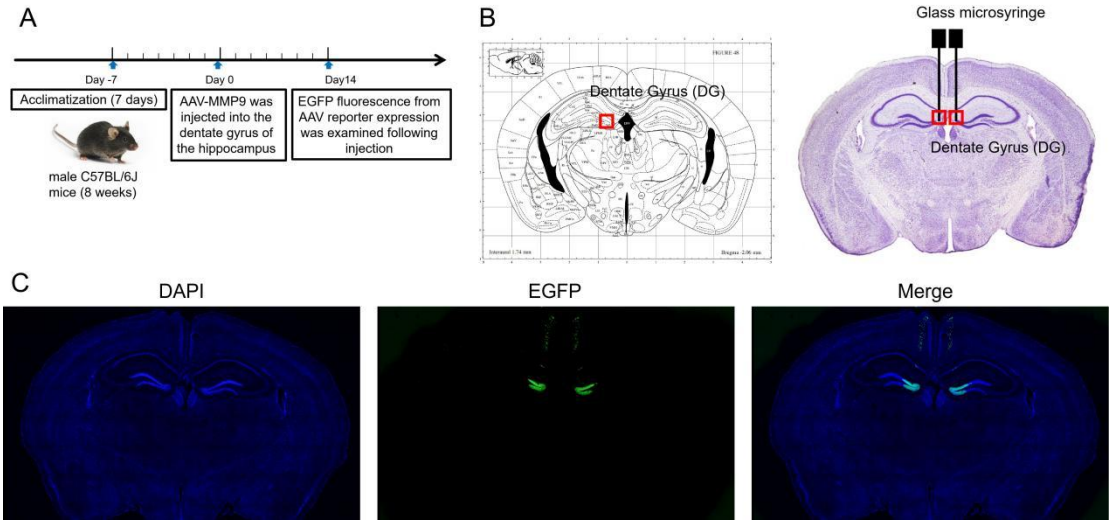


Figure S4. Experimental workflow and EGFP fluorescence validation of AAV-MMP9 injection in the mouse hippocampal dentate gyrus (DG)

(A) Schematic timeline of animal experiments. Eight-week-old male C57BL/6J mice were acclimated for 7 days. On day 0, AAV-MMP9 was stereotaxically injected into the hippocampal dentate gyrus. EGFP fluorescence expression of the AAV reporter gene was detected on day 14 after injection. (B) Schematic diagram of stereotaxic injection coordinates. A glass microsyringe was used for bilateral injection targeting the mouse hippocampal dentate gyrus (DG). (C) Representative fluorescence image showing EGFP reporter gene expression in the hippocampal dentate gyrus region. Nuclei were stained with DAPI.

References

1. GBD 2019 Mental Disorders Collaborators. Global, regional, and national burden of 12 mental disorders in 204 countries and territories, 1990-2019: a systematic analysis for the Global Burden of Disease Study 2019. Lancet Psychiatry 2022;9:137-150. doi:10.1016/s2215-0366(21)00395-3.

2. Ferrari AJ, Charlson FJ, Norman RE, Patten SB, Freedman G, Murray CJL, et al. Burden of depressive disorders by country, sex, age, and year: findings from the Global Burden of Disease Study 2010. PLoS Med 2013;10:e1001547. doi:10.1371/journal.pmed.1001547.

3. Friedrich MJ. Depression is the leading cause of disability around the world. JAMA 2017;317:1517. doi:10.1001/jama.2017.3826.

4. Wang PS, Berglund P, Olfson M, Pincus HA, Wells KB, Kessler RC. Failure and delay in initial treatment contact after first onset of mental disorders in the National Comorbidity Survey Replication. Arch Gen Psychiatry 2005;62:603-613. doi:10.1001/archpsyc.62.6.603.

5. Kessler RC, Bromet EJ. The epidemiology of depression across cultures. Annu Rev Public Health 2013;34:119-138. doi:10.1146/annurev-publhealth-031912-114409.

6. Chesney E, Goodwin GM, Fazel S. Risks of all-cause and suicide mortality in mental disorders: a meta-review. World Psychiatry 2014;13:153-160. doi:10.1002/wps.20128.

7. Cipriani A, Furukawa TA, Salanti G, Chaimani A, Atkinson LZ, Ogawa Y, et al. Comparative efficacy and acceptability of 21 antidepressant drugs for the acute treatment of adults with major depressive disorder: a systematic review and network meta-analysis. Lancet 2018;391:1357-1366. doi:10.1016/s0140-6736(17)32802-7.

8. Kapur S, Phillips AG, Insel TR. Why has it taken so long for biological psychiatry to develop clinical tests and what to do about it? Mol Psychiatry 2012;17:1174-1179. doi:10.1038/mp.2012.105.

9. Taylor MJ, Freemantle N, Geddes JR, Bhagwagar Z. Early onset of selective serotonin reuptake inhibitor antidepressant action: systematic review and meta-analysis. Arch Gen Psychiatry 2006;63:1217-1223. doi:10.1016/s0084-3970(08)70774-6.

10. Rush AJ, Trivedi MH, Wisniewski SR, Nierenberg AA, Stewart JW, Warden D, et al. Acute and longer-term outcomes in depressed outpatients requiring one or several treatment

steps: a STAR*D report. Am J Psychiatry 2006;163:1905-1917. doi:10.1176/ajp.2006.163.11.1905.

11. Trivedi MH, Rush AJ, Wisniewski SR, Nierenberg AA, Warden D, Ritz L, et al. Evaluation of outcomes with citalopram for depression using measurement-based care in STAR*D: implications for clinical practice. Am J Psychiatry 2006;163:28-40. doi:10.1176/appi.ajp.163.1.28.

12. Otte C, Gold SM, Penninx BW, Pariante CM, Ekin A, Fava M, et al. Major depressive disorder. Nat Rev Dis Primers 2016;2:16065. doi:10.1038/nrdp.2016.65.

13. Dantzer R, O'Connor JC, Freund GG, Johnson RW, Kelley KW. From inflammation to sickness and depression: when the immune system subjugates the brain. Nat Rev Immunol 2008;8:46-56. doi:10.1038/nrn2297.

14. Beurel E, Toups M, Nemeroff CB. The bidirectional relationship of depression and inflammation: double trouble. Neuron 2020;107:234-256. doi:10.1016/j.neuron.2020.06.002.

15. Heidt T, Sager HB, Courties G, Dutta P, Iwamoto Y, Zaltsman A, et al. Chronic variable stress activates hematopoietic stem cells. Nat Med 2014;20:755-761. doi:10.1038/nm.3589.

16. Mazza MG, Lucchi S, Tringali AGM, Rossetti A, Botti RE, Clerici M. Neutrophil/lymphocyte ratio and platelet/lymphocyte ratio in mood disorders: a meta-analysis. Prog Neuropsychopharmacol Biol Psychiatry 2018;84:229-236. doi:10.1016/j.pnpbp.2018.03.012.

17. Feng Z, Min L, Liang L, Chen B, Chen H, Zhou Y, et al. Neutrophil extracellular traps exacerbate secondary injury via promoting neuroinflammation and blood-spinal cord barrier disruption in spinal cord injury. Front Immunol 2021;12:698249. doi:10.3389/fimmu.2021.698249.

18. Raison CL, Rutherford RE, Woolwine BJ, Shuo C, Schettler P, Drake DF, et al. A randomized controlled trial of the tumor necrosis factor-alpha antagonist infliximab for treatment-resistant depression: the role of baseline inflammatory biomarkers. JAMA Psychiatry 2013;70:31-41. doi:10.1001/2013.jamapsychiatry.4.

19. Osimo EF, Baxter L, Lewis G, Jones PB, Khandaker GM. Prevalence of low-grade inflammation in depression: a systematic review and meta-analysis of CRP levels. Psychol

Med 2019;49:1958-1970. doi:10.1017/s0033291719001454.

20. Haapakoski R, Mathieu J, Ebmeier KP, Alenius H, Kivimaki M. Cumulative meta-analysis of interleukins 6 and 1beta, tumour necrosis factor alpha and C-reactive protein in patients with major depressive disorder. Brain Behav Immun 2015;49:206-215. doi:10.1016/j.bbi.2015.06.001.

21. Uher R, Tansey KE, Dew T, Maier W, Mors O, Hauser J, et al. An inflammatory biomarker as a differential predictor of outcome of depression treatment with escitalopram and nortriptyline. Am J Psychiatry 2014;171:31-38. doi:10.1176/appi.ajp.2014.14010094.

22. Pitman A, Suleman S, Hyde N, Hodgkiss A. Depression and anxiety in patients with cancer. BMJ 2018;361:k1415. doi:10.1136/bmj.k1415.

23. Cryan JF, Dinan TG. Mind-altering microorganisms: the impact of the gut microbiota on brain and behaviour. Nat Rev Neurosci 2012;13:701-712. doi:10.1038/nrn3346.

24. Masure S, Proost P, Van Damme J, Opdenakker G. Purification and identification of 91-kDa neutrophil gelatinase. Release by the activating peptide interleukin-8. Eur J Biochem 1991;198:391-398. doi:10.1111/j.1432-1033.1991.tb16027.x.

25. Huntley GW. Synaptic circuit remodelling by matrix metalloproteinases in health and disease. Nat Rev Neurosci 2012;13:743-757. doi:10.1038/nrn3320.

26. Meighan SE, Meighan PC, Choudhury P, Cryns VL, Mearow KM, Yavorska S, et al. Effects of extracellular matrix-degrading proteases matrix metalloproteinases 3 and 9 on spatial learning and synaptic plasticity. J Neurosci 2006;26:4143-4153. doi:10.1111/j.1471-4159.2005.03565.x.

27. Nagy V, Bozdagi O, Matynia A, Balcerzyk M, Okulski P, Dzwonek J, et al. Matrix metalloproteinase-9 regulates early phase reactions and long-term fear memory formation in the amygdala. Neuron 2006;51:551-564. doi:10.1523/jneurosci.4359-05.2006.

28. Rosenberg GA. Matrix metalloproteinases and their multiple roles in neurodegenerative diseases. Lancet Neurol 2009;8:205-216. doi:10.1016/s1474-4422(09)70016-x.

29. Yang Y, Estrada EY, Thompson JF, Liu W, Rosenberg GA. Matrix metalloproteinase-mediated disruption of tight junction proteins in cerebral vessels is reversed by synthetic matrix metalloproteinase inhibitor in focal ischemia in rat. J Cereb Blood Flow

Metab 2007;27:697-709. doi:10.1038/sj.jcbfm.9600375.

30. Rosell A, Cuadrado E, Ortega-Aznar A, Hernandez-Guillamon M, Lo EH, Montaner J. MMP-9-positive neutrophil infiltration is associated to blood-brain barrier breakdown and basal lamina type IV collagen degradation during hemorrhagic transformation after human ischemic stroke. Stroke 2008;39:1121-1126. doi:10.1161/strokeaha.107.500868.

31. Mizoguchi H, Nakade J, Tachibana M, Ibi D, Someya E, Koike H, et al. Matrix metalloproteinase-9 contributes to kindled seizure development in pentylenetetrazole-treated mice by converting pro-BDNF to mature BDNF in the hippocampus. J Neurosci 2011;31:12963-12971. doi:10.1523/jneurosci.3118-11.2011.

32. Alaiyed S, Bozzelli PL, Caccavano A, Wu JY, Conant K. Venlafaxine stimulates PNN proteolysis and MMP-9-dependent enhancement of gamma power; relevance to antidepressant efficacy. J Neurochem 2019;148:810-821. doi:10.1101/432419.

33. Moda-Sava RN, Murdock MH, Parekh PK, Fearey BC, Santini E, Song SC, et al. Sustained rescue of prefrontal circuit dysfunction by antidepressant-induced spine formation. Science 2019;364:eaat8078. doi:10.1126/science.aat8078.

34. Opdenakker G, Van den Steen PE, Dubois B, Nelissen I, Van Coillie E, Masure S, et al. Gelatinase B functions as regulator and effector in leukocyte biology. J Leukoc Biol 2001;69:851-859. doi:10.1189/jlb.69.6.851.

35. Lauhio A, Hastbacka J, Pettila V, Tervahartiala T, Karlsson S, Varpula T, et al. Serum MMP-8, -9 and TIMP-1 in sepsis: high serum levels of MMP-8 and TIMP-1 are associated with fatal outcome in a multicentre, prospective cohort study. Pharmacol Res 2011;64:590-594. doi:10.1016/j.phrs.2011.06.019.

36. Ahrens D, Koch AE, Pope RM, Stein-Picarella M, Niedbala MJ. Expression of matrix metalloproteinase 9 (96-kd gelatinase B) in human rheumatoid arthritis. Arthritis Rheum 1996;39:1576-1587. doi:10.1002/art.1780390919.

37. Sur Chowdhury C, Giaglis S, Walker UA, Buser A, Hahn S, Hasler P. Enhanced neutrophil extracellular trap generation in rheumatoid arthritis: analysis of underlying signal transduction pathways and potential diagnostic utility. Arthritis Res Ther 2014;16:R122. doi:10.1186/ar4579.

38. Pelus LM, Bian H, King AG, Fukuda S. Neutrophil-derived MMP-9 mediates synergistic mobilization of hematopoietic stem and progenitor cells by the combination of G-CSF and the chemokines GRObeta/CXCL2 and GRObetaT/CXCL2delta4. Blood 2004;103:110-119. doi:10.1182/blood-2003-04-1115.

39. Szklarczyk A, Lapinska J, Rylski M, McKay RDG, Kaczmarek L. Matrix metalloproteinase-9 undergoes expression and activation during dendritic remodeling in adult hippocampus. J Neurosci 2002;22:920-930. doi:10.1523/jneurosci.22-03-00920.2002.

40. Berman RM, Cappiello A, Anand A, Oren DA, Heninger GR, Charney DS, et al. Antidepressant effects of ketamine in depressed patients. Biol Psychiatry 2000;47:351-354. doi:10.1016/s0006-3223(99)00230-9.

41. Zarate CA Jr, Singh JB, Carlson PJ, Brutsche NE, Ameli R, Luckenbaugh DA, et al. A randomized trial of an N-methyl-D-aspartate antagonist in treatment-resistant major depression. Arch Gen Psychiatry 2006;63:856-864. doi:10.1001/archpsyc.63.8.856.

42. Daly EJ, Singh JB, Fedgchin M, Cooper K, Lim P, Winokur A, et al. Efficacy and safety of intranasal esketamine adjunctive to oral antidepressant therapy in treatment-resistant depression: a randomized clinical trial. JAMA Psychiatry 2019;76:399-409. doi:10.1001/jamapsychiatry.2017.3739.

43. Chen MH, Lin WC, Li CT, Wu HJ, Bai YM, Tsai SJ, et al. Effects of low-dose ketamine infusion on vascular endothelial growth factor and matrix metalloproteinase-9 among patients with treatment-resistant depression and suicidal ideation. J Psychiatr Res 2023;165:91-95. doi:10.1016/j.jpsychires.2023.07.022.

44. Ly C, Greb AC, Cameron LP, Wong JM, Barragan EV, Wilson PC, et al. Psychedelics promote structural and functional neural plasticity. Cell Rep 2018;23:3170-3182. doi:10.1016/j.celrep.2018.05.022.

45. Carhart-Harris R, Giribaldi B, Watts R, Baker-Jones M, Murphy-Beiner A, Murphy R, et al. Trial of psilocybin versus escitalopram for depression. N Engl J Med 2021;384:1402-1411. doi:10.1056/nejmoa2032994.

46. Goodwin GM, Aaronson ST, Alvarez O, Arden PC, Baker A, Bennett JC, et al. Single-dose psilocybin for a treatment-resistant episode of major depression. N Engl J Med

2022;387:1637-1648. doi:10.1056/nejmoa2206443.

47. Gasser P, Holstein D, Michel Y, Doblin R, Yazar-Klosinski B, Passie T, et al. Safety and efficacy of lysergic acid diethylamide-assisted psychotherapy for anxiety associated with life-threatening diseases. J Nerv Ment Dis 2014;202:513-520. doi:10.1097/nmd.0000000000000113.

48. Krasnova IN, Cadet JL. Methamphetamine toxicity and messengers of death. Brain Res Rev 2009;60:379-407. doi:10.1016/j.brainresrev.2009.03.002.

49. Martins T, Baptista S, Goncalves J, Leal E, Milhazes N, Borges F, et al. Methamphetamine transiently increases the blood-brain barrier permeability in the hippocampus: role of tight junction proteins and matrix metalloproteinase-9. Brain Res 2011;1411:28-40. doi:10.1016/j.brainres.2011.07.013.

50. Workman P, Aboagye EO, Balkwill F, Balmain A, Bruder G, Chaplin DJ, et al. Guidelines for the welfare and use of animals in cancer research. Br J Cancer 2010;102:1555-1577. doi:10.1038/sj.bjc.6605642.

51. O'Connor JC, Lawson MA, Andre C, Moreau M, Lestage J, Castanon N, et al. Lipopolysaccharide-induced depressive-like behavior is mediated by indoleamine 2,3-dioxygenase activation in mice. Mol Psychiatry 2009;14:156-164. doi:10.1038/sj.mp.4002148.

52. Biesmans S, Meert TF, Bouwknecht JA, Acton PD, Davoodi N, De Haes P, et al. Systemic immune activation leads to neuroinflammation and sickness behavior in mice. Mediators Inflamm 2013;2013:271359. doi:10.1155/2013/271359.

53. Daley JM, Thomay AA, Connolly MD, Reichner JS, Albina JE. Use of Ly6G-specific monoclonal antibody to deplete neutrophils in mice. J Leukoc Biol 2008;83:64-70. doi:10.1189/jlb.0407247.

54. Chiba S, Numakawa T, Ninomiya M, Richards MC, Wakabayashi C, Kunugi H. Chronic restraint stress causes anxiety- and depression-like behaviors, downregulates glucocorticoid receptor expression, and attenuates glutamate release induced by brain-derived neurotrophic factor in the prefrontal cortex. Prog Neuropsychopharmacol Biol Psychiatry 2012;39:112-119. doi:10.1016/j.pnpbp.2012.05.018.

55. Aschauer DF, Kreuz S, Rumpel S. Analysis of transduction efficiency, tropism and axonal transport of AAV serotypes 1, 2, 5, 6, 8 and 9 in the mouse brain. PLoS One 2013;8:e76310. doi:10.1371/journal.pone.0076310.

56. Autry AE, Adachi M, Nosyreva E, Na ES, Los MF, Cheng PF, et al. NMDA receptor blockade at rest triggers rapid behavioural antidepressant responses. Nature 2011;475:91-95. doi:10.1038/nature10130.

57. Roux F, Couraud PO. Rat brain endothelial cell lines for the study of blood-brain barrier permeability and transport functions. Cell Mol Neurobiol 2005;25:41-58. doi:10.1007/s10571-004-1376-9.

58. Kaech S, Banker G. Culturing hippocampal neurons. Nat Protoc 2006;1:2406-2415. doi:10.1038/nprot.2006.356.

59. Miltenyi S, Muller W, Weichel W, Radbruch A. High gradient magnetic cell separation with MACS. Cytometry 1990;11:231-238. doi:10.1002/cyto.990110203.

60. Swamydas M, Lionakis MS. Isolation, purification and labeling of mouse bone marrow neutrophils for functional studies and adoptive transfer experiments. J Vis Exp 2013;(77):e50586. doi:10.3791/50586-v.

61. Stewart SA, Dykxhoorn DM, Palliser D, Mizuno H, Yu EY, An DS, et al. Lentivirus-delivered stable gene silencing by RNAi in primary cells. RNA 2003;9:493-501. doi:10.1261/rna.2192803.

62. Nakagawa S, Deli MA, Nakao S, Honda M, Hayashi K, Nakaoke R, et al. A new blood-brain barrier model using primary rat brain endothelial cells, pericytes and astrocytes. Neurochem Int 2009;54:253-263. doi:10.1016/j.neuint.2008.12.002.

63. Tominaga H, Ishiyama M, Ohseto F, Sasamoto K, Hamamoto T, Suzuki K, et al. A water-soluble tetrazolium salt useful for colorimetric cell viability assay. Anal Commun 1999;36:47-50. doi:10.1039/a809656b.

64. Dehouck MP, Meresse S, Delorme P, Fruchart JC, Cecchelli R. An easier, reproducible, and mass-production method to study the blood-brain barrier in vitro. J Neurochem 1990;54:1798-1801. doi:10.1111/j.1471-4159.1990.tb01236.x.

65. Paschos NK, Brown WE, Eswaramoorthy R, Hu JC, Athanasiou KA. Advances in tissue

engineering through stem cell-based co-culture. J Tissue Eng Regen Med 2015;9:488-503. doi:10.1002/term.1870.

66. Wienken CJ, Baaske P, Rothbauer U, Braun D, Duhr S. Protein-binding assays in biological liquids using microscale thermophoresis. Nat Commun 2010;1:100. doi:10.1038/ncomms1093.

67. Can A, Dao DT, Arad M, Terrillion CE, Piantadosi SC, Gould TD. The mouse forced swim test. J Vis Exp 2012;(59):e3638. doi:10.3791/3638-v.

68. Liu MY, Yin CY, Zhu LJ, Zhu XH, Xu C, Luo CX, et al. Sucrose preference test for measurement of stress-induced anhedonia in mice. Nat Protoc 2018;13:1686-1698. doi:10.1038/s41596-018-0011-z.

69. Saper CB. A guide to the perplexed on the specificity of antibodies. J Histochem Cytochem 2009;57:1-5. doi:10.1369/jhc.2008.952770.

70. Sholl DA. Dendritic organization in the neurons of the visual and motor cortices of the cat. J Anat 1953;87:387-406.

71. Smith PK, Krohn RI, Hermanson GT, Mallia AK, Gartner FH, Provenzano MD, et al. Measurement of protein using bicinchoninic acid. Anal Biochem 1985;150:76-85. doi:10.1016/0003-2697(85)90442-7.

72. Taylor SC, Posch A. The design of a quantitative western blot experiment. Biomed Res Int 2014;2014:361590. doi:10.1155/2014/361590.

73. Boyum A. Isolation of mononuclear cells and granulocytes from human blood. Scand J Clin Lab Invest Suppl 1968;97:77-89.

74. Zheng GX, Terry JM, Belgrader P, Ryvkin P, Bent ZW, Wilson R, et al. Massively parallel digital transcriptional profiling of single cells. Nat Commun 2017;8:14049. doi:10.1038/ncomms14049.

75. Satija R, Farrell JA, Gennert D, Schier AF, Regev A. Spatial reconstruction of single-cell gene expression data. Nat Biotechnol 2015;33:495-502. doi:10.1038/nbt.3192.

76. Yu G, Wang LG, Han Y, He QY. clusterProfiler: an R package for comparing biological themes among gene clusters. OMICS 2012;16:284-287. doi:10.1089/omi.2011.0118.

77. Qiu X, Mao Q, Tang Y, Wang L, Chawla R, Pliner HA, et al. Reversed graph embedding

resolves complex single-cell trajectories. Nat Methods 2017;14:979-982. doi:10.1038/nmeth.4402.

78. Herzenberg LA, Tung J, Moore WA, Herzenberg LA, Parks DR. Interpreting flow cytometry data: a guide for the perplexed. Nat Immunol 2006;7:681-685. doi:10.1038/ni0706-681.

79. Buzsaki G, Draguhn A. Neuronal oscillations in cortical networks. Science 2004;304:1926-1929. doi:10.1126/science.1099745.

80. Hem A, Smith AJ, Solberg P. Saphenous vein puncture for blood sampling of the mouse, rat, hamster, gerbil, guinea pig, ferret and mink. Lab Anim 1998;32:364-368. doi:10.1258/002367798780599866.

81. Engvall E, Perlmann P. Enzyme-linked immunosorbent assay (ELISA). Quantitative assay of immunoglobulin G. Immunochemistry 1971;8:871-874. doi:10.1016/0019-2791(71)90454-x.

82. Makin TR, Orban de Xivry JJ. Ten common statistical mistakes to watch out for when writing or reviewing a manuscript. eLife 2019;8:e48175. doi:10.7554/elife.48175.

83. Casarotto PC, Girych M, Fred SM, Kovaleva V, Moliner R, Enkavi G, et al. Antidepressant drugs act by directly binding to TRKB neurotrophin receptors. Cell 2021;184:1299-1313.e19. doi:10.1016/j.cell.2021.01.034.

84. Schnitzer JE, Oh P, Pinney E, Allard J. Filipin-sensitive caveolae-mediated transport in endothelium: reduced transcytosis, scavenger endocytosis, and capillary permeability of select macromolecules. J Cell Biol 1994;127:1217-1232. doi:10.1083/jcb.127.5.1217.

85. Planas AM, Sole S, Justicia C. Expression and activation of matrix metalloproteinase-2 and -9 in rat brain after transient focal cerebral ischemia. Neurobiol Dis 2001;8:834-846. doi:10.1006/nbdi.2001.0435.

86. Justicia C, Panes J, Sole S, Cervera A, Deulofeu R, Chamorro A, et al. Neutrophil infiltration increases matrix metalloproteinase-9 in the ischemic brain after occlusion/reperfusion of the middle cerebral artery in rats. J Cereb Blood Flow Metab 2003;23:1430-1440. doi:10.1097/01.wcb.0000090680.07515.c8.

87. Barouch R, Appel E, Kazimirsky G, Brodie C. Macrophages express neurotrophins and

neurotrophin receptors. Regulation of nitric oxide production by NT-3. J Neuroimmunol 2001;112:72-77. doi:10.1016/s0165-5728(00)00408-2.

88. Fujimura H, Altar CA, Chen R, Nakamura T, Nakahashi T, Kambayashi J, et al. Brain-derived neurotrophic factor is stored in human platelets and released by agonist stimulation. Thromb Haemost 2002;87:728-734. doi:10.1055/s-0037-1613072.

89. Fridlender ZG, Sun J, Kim S, Kapoor V, Cheng G, Ling L, et al. Polarization of tumor-associated neutrophil phenotype by TGF-beta: "N1" versus "N2" TAN. Cancer Cell 2009;16:183-194. doi:10.1016/j.ccr.2009.06.017.

90. Li N, Lee B, Liu RJ, Banasr M, Dwyer JM, Iwata M, et al. mTOR-dependent synapse formation underlies the rapid antidepressant effects of NMDA antagonists. Science 2010;329:959-964. doi:10.1126/science.1190287.

91. Moliner R, Girych M, Brunello CA, Kovaleva V, Biojone C, Enkavi G, et al. Psychedelics promote plasticity by directly binding to BDNF receptor TrkB. Nat Neurosci 2023;26:1032-1041. doi:10.1038/s41593-023-01316-5.

92. Sohal VS, Zhang F, Yizhar O, Deisseroth K. Parvalbumin neurons and gamma rhythms enhance cortical circuit performance. Nature 2009;459:698-702. doi:10.1038/nature07991.

93. Williams LM. Precision psychiatry: a neural circuit taxonomy for depression and anxiety. Lancet Psychiatry 2016;3:472-480. doi:10.1016/s2215-0366(15)00579-9.

Declarations

Ethics approval and consent to participate

All animal experimental procedures were approved by the Animal Ethics Committee of National Key Laboratory of National Security Special Medicines (approval No. IACUC-DWZX-2025-601) and were conducted in accordance with the National Institutes of Health Guide for the Care and Use of Laboratory Animals. All procedures involving animals adhered to the sanctioned protocols and animal handling complied with the 3R principles governing laboratory animal ethics.

Competing interests

The authors declare that they have no competing interests.

Authors' contributions

Xia Li conceived and performed the experiments, analyzed the data, drafted the original manuscript. Tong Xu, Tianze Zhou, Weina Guo, Ziyi Wang contributed to animal model establishment, sample collection and molecular experiments. Jingcao Li and Qiongyin Fan assisted with bioinformatics analysis of single-cell RNA sequencing data and statistical analysis. Shuo Li and Shuaiming Zhu helped with in vitro blood–brain barrier model construction and immunofluorescence staining. Yang Zhang participated in data validation and manuscript revision. Rui Xue and Youzhi Zhang supervised the whole project, designed the research, reviewed and edited the manuscript. All authors read and approved the final manuscript.